



HAL
open science

Unveiling trends in soot nucleation and growth: When secondary ion mass spectrometry meets statistical analysis

Cornelia Irimiea, Alessandro Faccineto, Xavier Mercier, Ismael-Kenneth Ortega, Nicolas Nuns, Eric Therssen, Pascale Desgroux, Cristian Focsa

► To cite this version:

Cornelia Irimiea, Alessandro Faccineto, Xavier Mercier, Ismael-Kenneth Ortega, Nicolas Nuns, et al.. Unveiling trends in soot nucleation and growth: When secondary ion mass spectrometry meets statistical analysis. *Carbon*, 2018, 144, pp.815-830. 10.1016/j.carbon.2018.12.015 . hal-02298935

HAL Id: hal-02298935

<https://hal.science/hal-02298935>

Submitted on 27 Sep 2019

HAL is a multi-disciplinary open access archive for the deposit and dissemination of scientific research documents, whether they are published or not. The documents may come from teaching and research institutions in France or abroad, or from public or private research centers.

L'archive ouverte pluridisciplinaire **HAL**, est destinée au dépôt et à la diffusion de documents scientifiques de niveau recherche, publiés ou non, émanant des établissements d'enseignement et de recherche français ou étrangers, des laboratoires publics ou privés.

1 **Unveiling trends in soot nucleation and growth: when secondary ion mass**
2 **spectrometry meets statistical analysis**

3

4 **Author Affiliation.** Cornelia Irimiea^{1,2,†}, Alessandro Faccineto^{1,*}, Xavier Mercier¹,
5 Ismael-Kenneth Ortega³, Nicolas Nuns⁴, Eric Therssen¹, Pascale Desgroux¹, Cristian Focsa²

6 ¹Univ. Lille, CNRS, UMR 8522 - PC2A - Laboratoire de Physico-Chimie des Processus de Combustion et de
7 l'Atmosphère, 59655 Villeneuve d'Ascq, France.

8 ²Univ. Lille, CNRS, UMR 8523 - PhLAM - Laboratoire de Physique des Lasers, Atomes et Molécules, 59655
9 Villeneuve d'Ascq, France.

10 ³DMPE, ONERA, Univ. Paris Saclay, F-91123 Palaiseau, France.

11 ⁴Univ. Lille, CNRS, UMR 2638, Institut M. E. Chevreul, F-59000 Lille, France.

12 [†]Currently affiliated to ³.

13 *Correspondence to: alessandro.faccineto@univ-lille1.fr

14

15 ***Corresponding Author.** Alessandro Faccineto

16 Contact information: Tel: +33 (0)3 20 43 49 85, mail: alessandro.faccineto@univ-lille1.fr

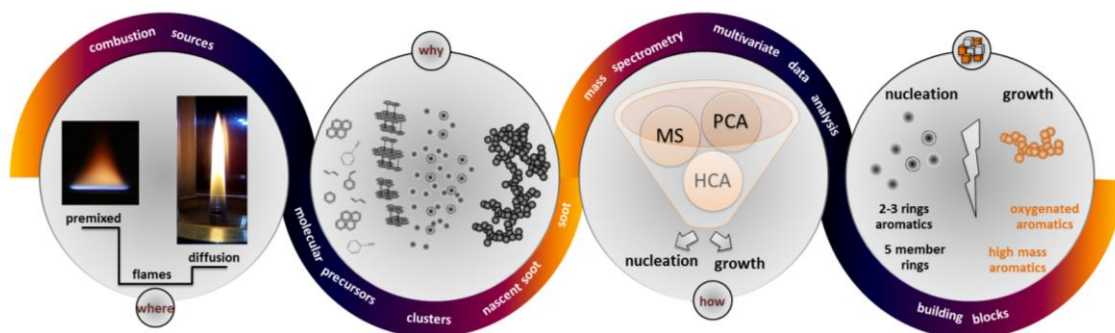
17

18 Unveiling trends in soot nucleation and growth: when
19 secondary ion mass spectrometry meets statistical
20 analysis

21 **Abstract (200 words max).** At the present day, ultrafine soot particles have become the
22 object of increasing attention due to their well-documented adverse effects on human health
23 and climate. In particular, understanding soot nucleation is one of the most challenging
24 problems toward a more controlled and cleaner combustion. Detailed information on the
25 chemistry of nascent soot particles (NSPs) is expected to provide clues on the soot formation
26 and growth reaction pathways. Herein, the early steps of soot formation in flames are
27 addressed by investigating the chemical composition of NSPs and their molecular precursors
28 by secondary ion mass spectrometry. The originality of this work lies on the combination of
29 several factors that include: two different approaches to gain access to soot nucleation in
30 premixed flames (analysis of a nucleation flame in which NSPs nucleate all along the reaction
31 coordinate without growing in size) and in diffusion flames (separation of the precursors and
32 soot regions); a sampling procedure that allows a rough separation of the condensable gas
33 phase from soot particles; a large database of collected samples and high mass resolution that
34 enable the use of an improved data reduction protocol based on hierarchical cluster analysis
35 and principal component analysis for the data mining and interpretation.

36

37 **Graphical abstract:**



38

39

40 **1. Introduction**

41 Soot nucleation is a term commonly used in combustion research to describe the transition
42 from molecular precursors in the gas phase to particulate matter in the condensed phase [1–5].
43 Soot nucleation is a wonderfully complex phenomenon that remains poorly understood to the
44 present day. The detection of the molecular precursors that participate to soot formation is a
45 major experimental challenge. In addition, the criteria used to identify soot particles in the
46 condensed phase are often based on the experimental measurements used to identify them,
47 thus over the years a variety of definitions partially overlapping or contradicting each other
48 arose [6–11]. The emission of thermal radiation is one of the possible criteria to identify
49 nascent soot particles (NSPs), which can be operationally defined as the smallest entities in
50 the condensed phase capable of emitting radiation described by Planck’s law (often cited as
51 blackbody-like or graybody radiation) [8]. Soot particles are generally at thermal equilibrium
52 with the combustion gas, and therefore emit thermal radiation in a continuous spectrum that
53 can be fitted with Planck’s law. This emission can be used to identify soot particles even as
54 their size approaches the limit of large organic molecules or small molecular clusters [12,13].
55 Hence, the yellow-orange luminosity of flames becomes an intuitive and effective criterion
56 for assessing the presence of soot particles, including NSPs that can be as small as 1-3 nm
57 diameter [6,14]. Although the detailed structure of NPSs remains essentially unknown, their
58 small size and the generally amorphous nature of young soot tend to suggest a disordered
59 rather than a core-shell internal nanostructure similar to mature soot primary particles [15–
60 17].

61 Despite many recent advances, the formation of NSPs from the gas phase remains an
62 elusive process. Mainstream hypotheses range from small aromatic molecules stacking into
63 progressively larger compact [18–20] or 3D cross-linked [21,22] clusters. However, because
64 of the intrinsic experimental difficulty in discerning the structure of NSPs, so far no
65 conclusive evidence could be provided to completely support or disprove one model. On the
66 molecular level, polycyclic aromatic hydrocarbons (PAHs) are long since well established
67 [23], from experiments [24–27] and modeling [28,29], to be important molecular building
68 blocks of soot. PAHs are found both in the gas phase as molecular precursors, and adsorbed
69 on the surface or integrated as structural elements in the nascent particles [30,31]. Recent
70 advances revealed for the first time the chemical structure of individual molecules found on
71 NSPs [32]. Experimental evidences that oxygen-containing hydrocarbons (OCHs) are

72 associated to soot have also been found [33], and thus they have been proposed as potential
73 candidates for soot nucleation in addition to PAHs [34,35]. The molecular precursors, and
74 more in general the compounds detected on freshly nucleated particles, typically feature high
75 hydrogen to carbon ratio $H/C > 0.8$ [15,16,36]. Once soot particles are formed, the soot mass
76 rapidly increases by surface growth, while the maturing primary particles coagulate and
77 coalesce to form progressively larger aggregates characterized by complex fractal-like
78 morphology [10,37]. In parallel, the H/C ratio of the compounds detected on the particles and
79 aggregates surface gradually decreases to values $H/C < 0.4$ typical of mature soot [25,9].

80 From the experimental point of view, NSPs are difficult to detect and their properties are
81 challenging to measure [26]. Commonly used diagnostics in combustion give access to a
82 variety of information that range from the soot volume fraction [38,39] to the particle size
83 distribution [6,40], structure and morphology [37,41]. The measurement of the mass of the
84 compounds in the gas phase or adsorbed on the particle surface provides important chemical
85 information on the species involved in soot formation and growth. As a result, countless
86 implementations of mass spectrometry exist that give access to the chemistry of both the gas
87 and the particulate phase [24,27,31,42–44]. In this work, we propose an innovative approach
88 based on ex-situ secondary ion mass spectrometry (SIMS) to probe the chemistry of soot
89 particles and condensable gas in parallel to obtain information on NSPs and their molecular
90 precursors. To achieve such goal, a method to separate the condensable gas from the soot
91 particles has been developed first [45]. Then, a large database of samples obtained in a variety
92 of experimental conditions has been analyzed. It is well known that mass spectrometry returns
93 large sets of data that have to be reduced into chemical information. Hence, data mining
94 becomes fundamental to extract hidden information [46,47]. Furthermore, increasing the size
95 of the database is arguably the most effective means of reducing and identifying sampling
96 errors and obtaining a stable and reliable factor analysis representative of the total population
97 [46]. The complementary information on the soot volume fraction profiles is obtained by
98 in-situ laser induced incandescence (LII) mapping [12] that relies on the enhancement of the
99 natural emission of soot particles in the flame by laser heating. Information on the spatial
100 distribution of the aromatic precursors in the gas phase is obtained by in-situ laser induced
101 fluorescence (LIF).

102 Isolating soot nucleation from other flame processes represents an additional challenge. In
103 particular, in sooting flames the chemical reactions occurring at the surface of particles tend to

104 build up as soon as NSPs are formed, and to quickly convert them into mature soot primary
105 particles, de facto concealing the nucleation process. In this work, to avoid such interference
106 and to identify independently the compounds involved in soot nucleation and growth,
107 different approaches based on the analysis of two low-pressure premixed and two atmospheric
108 diffusion laboratory methane flames are implemented. First, in the premixed nucleation flame,
109 a dynamic equilibrium between the processes that increase the soot particle size (nucleation,
110 surface growth, coagulation and coalescence) and those that decrease it (reversibility of
111 nucleation, surface oxidation) is reached by carefully choosing the flame equivalence ratio,
112 and results in the absence of any measurable increase in diameter of the NSPs against the
113 reaction time [8,48,49]. Thus, the comparison of the nucleation flame with a second sooting
114 flame stabilized in the same conditions represents a powerful tool to obtain information on the
115 chemistry of NSPs. Second, in the diffusion flames the formation regions of molecular
116 precursors and soot are separated and sufficiently far to be probed independently and with
117 little interference from one another.

118 A total of 152 samples are collected from the four laboratory flames at different reaction
119 times and analyzed by SIMS. Advanced statistical methods are employed to reduce this large
120 database and reveal similarity and specificity. The comparison of soot sampled from the
121 premixed and diffusion flames shows that PAHs and OCHs play a prominent role in soot
122 nucleation. In particular, the smallest compounds involved in soot nucleation are consistent
123 with PAHs having as few as 2-3 aromatic rings. Moreover, many strong signals come from
124 5-member ring PAHs, which further stresses the importance of these particular compounds.
125 The important role of the post-nucleation surface growth is isolated in the premixed flames
126 and leads to the definition of two distinct lists of compounds involved in the formation of
127 NSPs and their growth. The obtained data are compared to kinetic modeling in the literature
128 [50] showing that in the growth of both molecular precursors and compounds adsorbed on
129 soot, compact PAHs are preferred over open structures.

130 **2. Methodology**

131 **2.1. Burners and flames**

132 2.1.1. Premixed flames

133 Two low-pressure laminar, premixed, methane/oxygen/nitrogen flames are investigated
134 having equivalence ratio $\phi = 1.95$ (nucleation flame, PRE-N for short) and $\phi = 2.32$ (sooting
135 flame, PRE-S for short). Flame PRE-N and PRE-S were already object of investigations in the
136 past [51,14,8]. In particular, the soot volume fraction profiles of both flames are already
137 known [8]. Pictures of the flames are shown in Fig. 1a and b, while the flow conditions are
138 detailed in Table 1. The premixed flames are stabilized on a standard commercial Holthuis
139 (previously McKenna) burner equipped with a 60 mm diameter sintered bronze porous plug at
140 pressure $p = 267 \pm 1$ mbar and total gas flow $Q_{\text{tot}} = 3.96 \text{ L min}^{-1}$. The burner is installed on a
141 vertical linear translation stage located inside a low pressure vessel.

142 2.1.2. Sampling the premixed flames

143 A non-diluting quartz extractive microprobe enters the low-pressure vessel through the top
144 flange to reach the flames axially. The thin end of the probe has a 0.3 mm diameter aperture
145 that can be positioned in the flame with ± 0.1 mm accuracy. The probed flame depth is
146 estimated as twice the diameter of the probe aperture [52]. Changing the vertical position of
147 the burner changes the relative distance between the burner surface and the probe, and enables
148 positioning the tip of the probe at different height above the burner (HAB). Soot particles and
149 combustion gas are pumped, undiluted, through the probe and a heated (80°C) stainless steel
150 line to reduce condensation during the transfer to the sample holder. During the sampling, the
151 pressure inside the line is approximately 0.5 mbar. Flame PRE-S is sampled at six HABs on
152 the flame axis: before (7 mm) and at the beginning (9, 12 mm) of the soot incandescence
153 zone, and up to the burned gas region (15, 20, 40 mm). Flame PRE-N is sampled at the same
154 HABs.

155 2.1.3. Diffusion flames

156 Two atmospheric laminar diffusion methane flames are stabilized on a burner similar to
157 the one used by Siegmann et al. [53,54]. The configuration of the burner and more details on
158 the first flame (non-smoking flame, DIF-S for short) are given in Irimiea et al. [45]. A picture
159 of flame DIF-S is shown in Fig. 1c. The second diffusion flame (quenched flame, DIF-Q for
160 short), which features an additional quenching with argon in the reactive gas mixture, is used
161 as a reference since soot volume fraction and mass spectrometry data at different locations in
162 the flame axis are available in the literature [53,54]. Flame DIF-S is supplied with N5.0 grade

163 methane only (Q_{fuel}), while flame DIF-Q is supplied with a mixture of N5.0 grade methane
164 (Q_{fuel}) and argon (Q_{dil}) [53]. The flow conditions for the two diffusion flames are shown in
165 Table 2.

166 2.1.4. LII/LIF measurements on flame DIF-S

167 In-situ diagnostics commonly used for the detection of soot and precursors include optical
168 techniques as laser induced incandescence (LII) and laser induced fluorescence (LIF) that are
169 used to measure the soot volume fraction and the size of the primary particles [12,55,56] and
170 to map the molecular precursors in the gas phase [57], respectively. In this work, flame DIF-S
171 has been subject to detailed in-situ investigations since no information on the soot volume
172 fraction or on the chemical composition of the gas phase was available beforehand. Soot is
173 detected by LII at 1064 nm, while its precursors are detected by LIF at 488 nm and 266 nm
174 excitation wavelength. The fundamental of a pulsed Nd:YAG laser (Quantel Brilliant B, 6 ns
175 pulse width, 10 Hz) equipped with a frequency quadrupling module and an optical parametric
176 oscillator (Panther-EX OPO Continuum) pumped by the 3rd harmonic of a Nd:YAG laser
177 (Powerlight 8000 Continuum, 12 ns pulse width, 10 Hz) are used. Soot particles are heated
178 below their sublimation threshold ($F = 150 \text{ mJ cm}^{-2}$) and precursors in the gas phase are
179 excited without activating the incandescence of soot ($F = 7.7 \text{ mJ cm}^{-2}$ at 488 nm and
180 $F = 2.2 \text{ mJ cm}^{-2}$ at 266 nm). The LII/LIF emission is recorded at 90° incidence with respect to
181 the laser beam propagation, using a system of two achromatic lenses for the imaging of the
182 selected volume on the entrance of a spectrometer equipped with a 150 grooves mm^{-1} grating
183 blazed at 300 nm. A fast ICCD camera (Princeton Instruments 500PI MAX) placed at the exit
184 of the spectrometer records an image corresponding to 500 laser pulses. The LII/LIF detection
185 is performed during a 50 ns gate after the peak of the laser pulse. The spectral response of the
186 detection system is calibrated in intensity with an integration sphere (SphereOptics CSTM-
187 LR-6-M), while the wavelength calibration is performed with an Hg-Ar pen-ray line source.
188 The LII signal is integrated over a 5 nm wavelength window centered at 750 nm, while the
189 Vis-LIF and UV-LIF signals are integrated over the same spectral window centered at
190 550 nm. The LII and LIF signals are recorded at different HAB by translating the flame on the
191 vertical axis. The emission of the flame is subtracted from each LII/LIF image, and the
192 LII/LIF signal is normalized to the maximum detected value. It is therefore possible to
193 localize and distinguish between the gas phase precursors and soot particles. A schematic
194 representation of the setup is shown in Fig. 2a, while Fig. 2b shows the evolution of the

195 LII/LIF against HAB. In flame DIF-S, the UV-LIF signal is detected very low in the flame
196 from around 5 mm HAB, it increases up to a maximum at 50 mm HAB, and finally disappears
197 above 70 mm HAB. The Vis-LIF signal starts at 20 mm, reaches a maximum at 65 mm HAB
198 and completely disappears at 85 mm HAB. The LII signal starts at 62 mm HAB, very close to
199 the maximum of the Vis-LIF, reaches a maximum at 80 mm HAB, then quickly decreases and
200 disappears around 105 mm HAB. Both diffusion flames are non-smoking.

201 2.1.5. Sampling the diffusion flames

202 Flame DIF-S is characterized by LII/LIF herein to select the optimal HABs for the
203 sampling, while flame DIF-Q is used as a reference since the soot profile and mass
204 spectrometry data at different locations in the flame axis are available in the literature [53,54].
205 The extraction system is detailed in [45]. Briefly, it consists of a sampling probe having
206 0.25 mm diameter aperture coupled to an automatic pressure regulation system inserted
207 radially into the flame, engineered to combine high dilution ratio up to 3×10^4 [40] while
208 minimizing flame perturbations [58]. The diffusion flames are sampled at three HABs each in
209 the flame axis, at the maximum of the UV fluorescence detected by LIF (48 mm for flame
210 DIF-S and 25 mm for flame DIF-Q), at the beginning of the soot incandescence zone (65 mm
211 for flame DIF-S and 45 mm for flame DIF-Q), and near the maximum of the soot
212 incandescence zone in a region with weak signal of fluorescent species excited by visible
213 wavelength (80 mm for flame DIF-S and 55 mm for flame DIF-Q). The large soot volume
214 fraction of the diffusion flames requires dilution during sampling to quench chemical
215 reactions and limit particle coagulation and coalescence.

216 2.2. Preparation of the samples and SIMS measurements

217 Online and ex-situ diagnostics often depend on mass spectrometry to gather chemical
218 information from the samples. Online techniques relying on the generation and analysis of a
219 molecular beam have been available for almost two decades now [42,59]. Their modern
220 implementations, like aerosol mass spectrometry for instance, are now compact and
221 commercially available devices that can provide semi-quantitative measurements in real time
222 and therefore have become widespread for the analysis of environmental samples [60–64].
223 The applications of surface techniques to the ex-situ analysis of soot are too many to describe
224 herein, and range from thermal [65,66] to laser desorption mass spectrometry [67], possibly

225 after solvent extraction [43] and on a variety of deposition substrates [27,44,68]. SIMS has
226 been independently used for the analysis of the chemical composition of aerosols [69,70] and
227 PAH containing samples [71], although it never was the technique of choice for systematic
228 investigations of the chemical composition of soot particles.

229 In this work, samples obtained by impaction of soot and condensable gas on silicon and
230 titanium wafers are characterized using the ToF.SIMS⁵ instrument available at the Regional
231 Platform of Surface Analysis at the University of Lille. A detailed description of the adopted
232 analytical protocol is provided in Irimiea et al. [45]. SIMS is a high sensitivity analytical
233 technique used to determine the chemical composition of unknown samples that can probe a
234 surface layer thinner than 1 nm. The sample is sputtered with a primary ion beam and the
235 ejected secondary ions are mass-analyzed with a time of flight mass spectrometer having
236 maximum resolving power $\sim 10^4$. The distinction between soot and the condensable gas phase
237 is obtained by following the protocol proposed in Irimiea et al. [45]. During impaction
238 deposition, particles deposit preferentially at the outlet of the impactor, while condensable gas
239 diffuse all over the wafer surface, including the already deposited soot. The mapping of the
240 sample surface and the comparison of the mass spectra of the soot impacting region and
241 surroundings by image reconstruction can be exploited to get information on the chemical
242 composition of the two phases.

243

244 **2.3. HCA and PCA in a nutshell**

245 Mass spectra of soot contain a significant amount of chemical information that is
246 difficult to extract because of the large number of signals they typically feature [72]. As high
247 resolving power mass spectrometers get easier and easier to access, advanced statistical tools
248 have become invaluable to refine large databases of raw mass spectra and to reduce them into
249 chemical information. Principal component analysis (PCA) is used to classify the data and
250 explain the variance of the database. Since PCA is based only on a fraction of the total
251 variance, its output can be affected by the presence of outliers. Therefore, to increase the
252 confidence level of the data reduction, hierarchical clustering analysis (HCA), which is based
253 on the total variance of the dataset, is applied in parallel following the approach proposed by
254 Pei et al. [73].

255 HCA attempts to build a hierarchy of clusters of observations based on their similarity.
256 A measure of the similarity between clusters and a set of linkage criteria are required to
257 decide which clusters should be combined, and can be provided in a variety of different ways
258 conceptually based on the calculation of the distance between pairs of observations. For
259 instance, a common approach is based on Euclidian distances between observations, then
260 HCA is computed with the group average method. The average linkage criterion is commonly
261 used because is space-conserving and delivers the most robust data hierarchy after using a
262 multitude of algorithms [73,74]. The results of HCA are organized in distinctive-looking tree
263 diagrams (dendrograms) that show the distances at which the data clusters are merged.

264 PCA is a mathematical tool used in exploratory data analysis to identify relatedness
265 among populations [75,76]. In PCA, an original set of possibly correlated variables is
266 transformed into a second set of linearly uncorrelated variables (principal components) that
267 retains the maximal amount of information of the original data. PCA is performed on a data
268 correlation or covariance matrix usually after a normalization of the original data to zero
269 average and unit variance. The normalization is a particularly delicate step since PCA only
270 uses linear transformations, and therefore PCA on a non-normalized dataset would be
271 dominated by the largest numeric values. The percentage of the total variance explained by
272 each principal component is stored in the eigenvalues and visualized in the *scree plot*
273 (eigenvalues against principal components). Essentially, the scree plot orders the eigenvalues
274 from the largest to the smallest, and it is often used to select the number of principal
275 components to be further considered. The relative weights of each original variable used to
276 calculate the principal components are stored in the eigenvectors and visualized in the *loading*
277 *plots* (weights against original variables). The loading plots are fundamental to quickly
278 identify which variables affect each principal component. The loadings can take negative or
279 positive value: the more a variable influences one of the principal components, the larger the
280 corresponding loading in absolute value. Conversely, the less a variable influences one of the
281 principal components, the closer the corresponding loading is to zero. The scores are linear
282 combinations of the data calculated from the coefficients for each principal component, and
283 represent the distance of an observation from a principal component. There is one score for
284 each observation in the data set and for each principal component. A *score plot* shows the
285 scores of two principal components one against the other, and can be used as a base to classify
286 the data. For instance, if the first two components account for the largest part of the variance

287 of the database, the PC2 against PC1 score plot is generally sufficient to identify data clusters
288 and trends.

289 In this work, HCA and PCA are implemented on the normalized integrated peaks outcome
290 of the mass spectra. The peak ion counts are normalized by the total ion count of each
291 spectrum after background removal. Then, they are organized in a matrix containing the
292 observation (rows) by the peak ion counts (columns). Finally, HCA (group average clustering
293 method, Euclidean distances) and PCA (covariance matrix) are implemented on the data
294 matrix. Routines in OriginPRO 2016 (OriginLab, Northampton, U.S.A.), Matlab
295 (MathWorks, Natick, U.S.A.) and the freeware ToFTools have been used for the peak
296 deconvolution and computation of the statistical methods.

297 **3. Results and discussion**

298 **3.1. Understanding the mass spectra**

299 A selection of the recorded mass spectra sorted by flame (rows) and sampling HAB
300 (columns) is shown in Fig. 3. The mass spectra of the condensable gas phase and soot are
301 shown in the top and bottom panels, respectively. The mass spectra feature a quasi-bimodal
302 distribution of peaks separated by a gap around m/z 150-200. The first mode spans m/z 0-150
303 and its strongest signals are attributed to fragment ions as discussed below. This mode tends
304 to be more prominent in the condensable gas sampled at high HAB, and in flame PRE-N at
305 any HAB. The second mode roughly spans m/z 150-800 and features signals mainly attributed
306 to $C_mH_n^+$ and $C_mH_nO_p^+$ molecular ions. The second mode is more prominent in the diffusion
307 than the premixed flames. The relative intensity of the peaks and the position of the modes in
308 the m/z axis are both flame and HAB dependent. Within the modes, the signal peaks always
309 recur in groups corresponding to the increasing number of carbon atoms m . Each group
310 contains several peaks corresponding to ions having a progressively increasing number of
311 hydrogen atoms n . Neighboring groups are separated by gaps in which weaker but still well
312 resolved peaks are detected. The gaps become progressively smaller as m/z increases, and
313 disappear from m/z 700 upwards.

314 The analytical protocol adopted in our previous work and based on soot and condensable
315 gas deposition by impaction [45] results in a mass resolution ($m/\Delta m \sim 7000$) large enough to
316 enable using mass defect analysis for the identification of unknown molecular ions. Despite
317 being richer in low mass signals, the SIMS mass spectra well match our previous two-step
318 laser mass spectrometry (L2MS) measurements [27] and early tests with SIMS where
319 deposition on filters was used [8]. The strongest peak in a group sharing the same m depends
320 on the parity of m . If m is even, then the strongest peaks have even nominal mass, while if m
321 is odd, then the strongest peaks have odd nominal mass. This behavior is consistent with the
322 attribution of the signal peaks to PAH ions. In fact, odd m PAHs contain (at least) one
323 non-aromatic carbon atom, and therefore post-ionization hydrogen elimination reaction result
324 in increased stability by extended electron resonance.

325 Flame DIF-Q is similar to the work of Siegmann et al. [53,54] and provides a comparison
326 with the literature. In this work, a significant extension of the upper mass limit could be
327 obtained in a range important for the nucleation and growth of NSPs. Although the peak

328 relative intensities are significantly different in the two works, the main mass sequences
329 attributed to benzenoid PAHs are well consistent. The peak relative intensities are
330 characteristic of the ionization scheme. In Siegmann et al. [54], resonant enhanced
331 multiphoton ionization (REMPI) is used that enables the efficient ionization and hence a
332 highly selective detection of resonant compounds. In particular, ionization at 248 nm
333 excitation wavelength is very effective for the detection of PAHs in the range m/z 200-300
334 [77], and the obtained distribution of peaks is centered around m/z 200 consistently with
335 REMPI of low mass PAHs. Furthermore, the smooth energy transfer typical of low irradiance
336 laser ionization greatly limits post-ionization dissociation, resulting in almost fragment free
337 mass spectra. This is a major difference with SIMS, where the harsher ionization produces
338 fragment-rich mass spectra.

339 In this work, peaks are identified and assigned a molecular formula based on their mass
340 defect [78]. A working peak list containing 771 peaks is generated following the protocol
341 established in Irimiea et al. [45]. Only peaks having signal-to-noise ratio (SNR) larger than
342 three times the standard deviation of the background noise are included in the data reduction.
343 One mass spectrum and the corresponding mass defect plot are shown as examples in Fig. 4a
344 and b, respectively. High mass defect ions are identified as $C_mH_n^+$ from their typical pattern
345 and assigned a molecular formula. The difference between the measured accurate mass and
346 the exact mass of the assigned molecular formula is typically in the 0.1-5 ppm range. A large
347 number of weaker signals characterized by lower mass defect are also detected and attributed
348 to OCHs .

349 SIMS analyses are often affected by post-ionization dissociation reactions that generate a
350 potentially large number of fragment ions and increase the complexity of the mass spectra.
351 Fragment ions should be identified and treated independently of the molecular ions. To this
352 end, hierarchical clustering analysis (HCA, group average clustering method, Euclidean
353 distances) is used to find general trends and similarities in the behavior of the peak signals,
354 and to search correlations between individual peaks and/or groups of peaks. HCA found three
355 main clusters of peaks that share close behavior that are shown in different colors in Fig. 4a
356 and b. Cluster 1 (black data) only contains low mass defect ions that are easily identified
357 thanks to their distinctive pattern in the mass defect plot. Their mass defect is too low to be
358 consistent with molecular ions (strongest signals are C_mH^+ , $C_mH_2^+$ and $C_mH_3^+$, $m \in [1, 16]$).
359 Cluster 2 (red data) contains higher mass defect ions that have mass consistent with

360 unsaturated and aromatic compounds. It is worth to notice that many small PAHs from $C_9H_8^+$
361 up to $C_{24}H_{16}^+$ are in cluster 2. Finally, cluster 3 (green data) contains signals only attributed
362 by mass defect analysis to large PAHs and OCHs. The three clusters coexist in m/z 200-300.
363 At lower m/z , clusters 1 and 2 dominate, while the vast majority of signals at higher m/z are
364 part of cluster 3. The peak intensity scatter matrix gives further information on the correlation
365 coefficients (Pearson's R^2) calculated on the normalized peak intensities. The peaks classified
366 by HCA in the same cluster are highly correlated to each other ($R > 0.8$). The peaks classified
367 in clusters 1 and 2 are generally anti-correlated to those classified in cluster 3, but feature
368 much weaker correlation coefficients ($-0.7 < R < 0.1$) than the previous case. In particular, it is
369 interesting to notice that the anti-correlation of clusters 1 and 3, together with the very low
370 mass defect of the peaks in cluster 1, can be explained in terms of post-ionization dissociation
371 reactions. Dissociation reactions remove molecular ions from the ion plume, therefore the
372 higher the counts of fragment ions (cluster 1) and the lower the counts of precursor ions
373 (cluster 3), and vice versa. The negative correlation between clusters 2 and 3 is more difficult
374 to explain as it does not seem to be related to the analysis process, and likely have a more
375 fundamental explanation (for instance, small hydrocarbons in cluster 2 might be depleted to
376 generate the larger species in cluster 3). In any case, this result greatly strengthens the
377 hypothesis that different compounds are involved in different processes, and that advanced
378 statistical analysis is necessary to classify the different behaviors in view of finding a detailed
379 explanation.

380 **3.2. From peaks to molecules**

381 Once attributed a molecular formula based on their mass defect, $C_mH_n^+$ ions can be
382 represented as points of coordinates ($n/m, m/z$) in a two-dimensional space. The resulting
383 graphs are an adaptation of the well known C-H diagrams [79], and are especially useful in
384 this context as they provide the space of all possible combinations of (n, m) and an
385 immediate, visual feedback on the molecular formula of all detected ions. Furthermore, C-H
386 diagrams are a convenient way to compare experimental results with the predictions of kinetic
387 modeling [80]. Fig. 5 shows the data reduced from the mass spectra in Fig. 3 sorted by flame
388 and sampling HAB. The n/m ratio roughly spans the range [0.2, 0.8], clearly decreasing as
389 m/z increases. The molecular formulae $C_mH_n^+$ obtained from the mass defect analysis are
390 consistent with PAHs that contain 5- and 6- member rings and side-substituted PAHs. In Fig.
391 5, the PAH distributions are compared with the model proposed by D'Anna et al. [50] to

392 follow the molecular growth in terms of C and H atom numbers. The black dashed lines
393 represent the limits of benzene oligomers (top line, high n/m) and pericondensed PAHs
394 (bottom line, low n/m). In all flames, the identified $C_mH_n^+$ ions are found scattered between
395 the benzene oligomers and the pericondensed PAHs limits, generally much closer to the latter.
396 The few data points found below the pericondensed PAHs limit are possibly fragment ions
397 not identified by HCA as discussed above, or alternatively substituted PAHs or pericondensed
398 PAHs with additional 5-member rings on a zigzag edge. Soot sampled from flame PRE-N
399 only shows signals up to m/z 400-450, while soot sampled from the other three flames shows
400 signals up to m/z 850-900.

401 The position in a mass spectrum at which the ion SNR falls below 3 is denoted as $(m/z)_{\max}$
402 and is a convenient variable to monitor the mass sequence. As shown in Fig. 6, $(m/z)_{\max}$
403 depends on the flame type, sampling HAB and analyzed zone (condensed gas phase or soot).
404 In Fig. 6, the filled dots represent soot while empty dots represent the condensable gas phase
405 obtained in the absence of soot (for instance, flames PRE-S at $HAB \leq 9$ mm or PRE-N at any
406 HAB) or by image reconstruction whenever soot coexists with the gas phase (for instance,
407 flames DIF-S and DIF-Q at 65 and 45 mm HAB, respectively).

408 In flame PRE-N (nucleation flame) no differences are observed between condensable gas
409 and soot samples, and additionally little to no evolution against HAB is observed as shown in
410 Fig. 6a. This absence of net molecular growth is consistent with a soot formation mechanism
411 driven by the generation of NSPs all along the flame reaction coordinate and by the virtual
412 absence of soot particle size increase [8]. The existence in flame PRE-N of PAHs up to m/z
413 400-450 in parallel to NSPs detected by LII further supports the hypothesis that soot
414 nucleation in premixed flames does not require large hydrocarbons to occur. On the other
415 hand, $(m/z)_{\max}$ obtained from the analysis of soot and condensable gas in flame PRE-S greatly
416 differ. As shown in Fig. 6b, $(m/z)_{\max}$ of the condensable gas features a local maximum at
417 12-15 mm HAB that corresponds to the beginning of the soot nucleation zone determined by
418 LII (gray highlighted region). Then, $(m/z)_{\max}$ progressively decreases as the HAB further
419 increases down to the same value of flame PRE-N at 40 mm HAB. $(m/z)_{\max}$ of soot starts at
420 m/z 850-900 at the beginning of the nucleation zone, then progressively decreases against
421 HAB. The diffusion flames reveal a different evolution of $(m/z)_{\max}$ than the premixed flames
422 as shown in Fig. 6c and d. Signals up to m/z 850-900 are identified upstream the soot

423 inception zone in both diffusion flames from very low HAB. At higher HAB, $(m/z)_{\max}$
424 monotonically decreases, faster in the condensable gas than in soot.

425 **3.3. Disclosing the chemistry of soot nucleation and growth**

426 HCA and PCA are used to find correlations between subsets of the total sample
427 population. HCA and PCA are initially used to refine the complete dataset of 152 samples,
428 and in particular to identify sampling and analysis artefacts. A detailed discussion can be
429 found in the Supporting Information (*SI. Local factors affecting the structure of the*
430 *database*), while herein a reduced dataset of 101 samples obtained after removal of the
431 identified artefacts is discussed.

432 Fig. 7a and b compare the HCA dendrogram to the PC2 vs. PC1 score plot obtained after
433 removing the identified fragment ions. The loading plots of PC1 and PC2 are shown in Fig. 7c
434 and d, respectively. The loadings correspond to signals attributed by mass defect analysis to
435 PAHs and OCHs, and are represented by black and red data, respectively. To provide an
436 immediate visual feedback, the data clusters identified by HCA are color coded to match the
437 groups of samples in the PCA score plot. It is significant that the cluster structure identified
438 by HCA and PCA are consistent and all data clusters are well separated and appear adjacent
439 to each others in the score plot. The correspondence of the data clusters with the samples is
440 further elaborated in Table 3. In the score plot and dendrogram, samples from different flames
441 and HABs are most of the times classified in independent data clusters. For instance, data
442 clusters 1, 2 and 8 only contain samples from the diffusion flames, both condensable gas at
443 low HAB (data cluster 1), and young and mature soot at higher HAB (data clusters 2 and 8).
444 Data clusters 3, 4 and 7 contain soot samples from flame PRE-S well separated by HAB. Data
445 cluster 5 contains all the samples characterized by high negative loadings of PC1 in the low
446 m/z region, and low negative loadings in the high m/z region of PC2 as shown in Fig. 7c and
447 d. Data cluster 5 notably includes the majority of samples from flame PRE-N, the
448 condensable gas from the tip of the diffusion flames and all samples from flame PRE-S at
449 40 mm HAB despite originating from very different combustion conditions. Finally, data
450 cluster 6 contains all the samples characterized by high negative loadings of PC1 in the low
451 m/z region, and positive loadings in the low m/z region of PC2 as shown in Fig. 7c and d.
452 These samples include all the condensable gas from flame PRE-S except 40 mm HAB, and

453 flame PRE-N at 40 mm HAB. Two samples from flame PRE-N at 15 mm HAB are also in
454 this data cluster.

455 PC1 (52.6%) and PC2 (23.5%) are by far the most interesting principal components of
456 PCA that together explain the 76.1% of the variance of the database. The lower variance
457 principal components (PC3, PC4, etc.) are not considered in the discussion. A sharp change of
458 sign of PC1 occurs at m/z 165–245. PC1 > 0 contains signals attributed to PAHs and OCHs,
459 while PC1 < 0 contains signals attributed to low mass PAHs. PC2 shows a much slower
460 change of sign in m/z 294–450. The loadings on PC2 > 0 are much larger than PC2 < 0 and
461 mostly contain signals attributed to PAHs, while the loadings on PC2 < 0 are closed to zero
462 and mainly attributed to OCHs. The highest loading of PC1 > 0 is m/z 239.086 ($C_{19}H_{11}^+$), and
463 the highest loading of PC1 < 0 is m/z 115.055 ($C_9H_7^+$). In the ionization conditions the
464 experiments are performed, post-ionization H-elimination reactions of more than two
465 hydrogen atoms are never observed during the analysis of analytical standards (pure PAHs),
466 and therefore these signals are attributed to the product of H-elimination from $C_{19}H_{12}^+$ and
467 $C_9H_8^+$, respectively. Many similar cases exist in the mass spectra. It is worth to notice that odd
468 numbers of carbon atoms are compatible with polyaromatic structures containing 5-member
469 ring(s), at least one non-aromatic carbon atom, or both. The existence of such signal as base
470 peak is remarkable given the general higher thermodynamic stability of benzenoid PAHs [23],
471 and suggests that structures containing 5-member rings or non-aromatic carbon atoms play an
472 important role on soot formation and growth and are stable enough to be found in the gas
473 phase or adsorbed on young soot particles at potentially large concentration. This has been
474 very recently confirmed by a combined experimental and theoretical study [81]. Whether
475 chemical species that are removed from the flame still carry information on the flame
476 processes remains a central problem of the data interpretation. The extraction procedure in
477 ex-situ diagnostics causes irreversible modifications to the samples. Recombination reactions
478 result in the loss of all information on reactive species (radicals, ions) as soon as they are
479 extracted from the flame, and furthermore volatile compounds partially desorb in the mass
480 spectrometer during the creation of the vacuum before the mass analysis can take place. On
481 the other hand, by applying high dilution factors during sampling, extensive post-sampling
482 recombination can be avoided. Regardless, the good agreement of the sequence of
483 hydrocarbons detected on any sampling conditions with the prediction of kinetic modeling is a
484 strong evidence that at least the information on the large hydrocarbons, in the gas phase or

485 adsorbed at the particle surface, is preserved, and this information can be linked to the
486 composition of the particulate matter (NSPs and primary soot particles).

487 To help explaining the results of PCA it is generally helpful to add as much information as
488 it is available to the score plots. Fig. 8 shows the PC2 vs. PC1 score plot with data classified
489 by flame and sampling HAB. The data point color and shape represent the sampled flame,
490 PRE-N (red rounds), PRE-S (violet stars), DIF-S (green squares) and DIF-Q (blue triangles)
491 while the data point interior represents soot (filled dots) and condensable gas (empty dots).
492 PC1 and PC2 are the most important principal components that explain the 52.6% and the
493 23.5% of the total variance of the database, respectively:

- 494 • PC1 < 0 (m/z 93-245) identifies samples that contain very small carbon-based
495 clusters and/or nanoparticles in the gas phase (Fig. 7). Notably, such entities
496 include NSPs from flame PRE-N resulting from the nucleation process and having
497 constant size all along the flame axis. Furthermore, PC1 < 0 contains soot
498 nanoparticles resulting from the re-oxidation of larger soot aggregates occurring at
499 high HAB in the diffusion flames (80 mm in DIF-S and 55 mm in DIF-Q, both
500 diffusion flames are non-smoking).
- 501 • PC1 > 0 (m/z 165-731) is characterized by high loadings of PAHs with more than
502 three aromatic rings (Fig. 7), and its most remarkable feature is being clearly
503 linked to the analysis of visible soot deposits and to the low HAB samples from
504 the diffusion flames (48 mm in DIF-S and 25 mm in DIF-Q in Fig. 8). The high
505 loadings of PC1 > 0 point to the existence of large PAHs upstream the soot
506 nucleation region in the diffusion flames, but not in the premixed flames. The high
507 scores obtained for the gas phase in flames DIF-S and DIF-Q confirms the
508 predominance of aromatic compounds with mass in the range m/z 165-731 well
509 below the soot inception zone. The lower scores on PC1 obtained for samples
510 collected in a sooting region imply that these compounds are consumed or
511 converted as the HAB increases. This phenomenon is reversed in flame PRE-S, in
512 which high mass compounds are found on soot rather than in the gas phase.
- 513 • PC2 < 0 (m/z 294-731) contains all samples of flame PRE-N except 40 mm HAB
514 and all the condensable gas from the tip of the other three flames at high HAB
515 (PC1 < 0), and samples not clearly clustered of flames PRE-S, DIF-S and DIF-Q
516 (PC1 > 0). The very small loadings of PC2 < 0 (Fig. 7) indicate that no statistically

517 significant differences exist between samples with high score in $PC2 < 0$, and that
518 the corresponding variables are not involved in the phenomenon described by $PC2$.
519 This is particularly interesting for data clusters 2 and 5 that contain samples
520 obtained from several flames. In Table 4, the structure of data cluster 2 suggests
521 that soot obtained from the tip of the two diffusion flames has virtually the same
522 composition despite the different flame height. However, data cluster 5 contains a
523 larger variety of samples having in common very low concentration of high mass
524 PAHs. As shown in Table 4, these samples include flame PRE-N at all HAB
525 except 40 mm, flame PRE-S at 40 mm, and all condensable gas sampled from the
526 tip of the diffusion flames.

527 • $PC2 > 0$ (m/z 90-450) contains well separated condensable gas samples of flame
528 PRE-N at 40 mm HAB and all the condensable gas of flame PRE-S ($PC1 < 0$), and
529 again samples not clearly clustered from flames PRE-S, DIF-S and DIF-Q
530 ($PC1 > 0$). It is interesting to notice how a slight increase of the peak intensity in
531 the mass spectra collected in flame PRE-N at 40 mm HAB, but not of $(m/z)_{max}$,
532 ultimately results in this HAB to be the only one to appear in $PC2 > 0$. Among
533 other things, this shows that PCA is sensitive to small changes of the peak
534 intensity.

535 The data collected at all HABs except 40 mm in flame PRE-N coexist in the same data
536 cluster, i.e. no statistically significant differences in the mass spectra can be observed at
537 different HABs. We believe this to be a potentially important finding. Flame PRE-N is
538 characterized by the existence of NSPs having nearly constant diameter in the range of 1-3 nm
539 all along the reaction coordinate as already established by in-situ LII investigations [14,48,51]
540 and supported by kinetic modeling [49]. The lack of particle size growth and the very slow
541 evolution of the soot chemical composition as shown by the SIMS analysis strongly point
542 toward the formation of a steady state for both the particle size and their chemical
543 composition. After the particle formation and initial growth, the surface oxidation processes
544 become progressively more important as the particle grows in size. At some point, the overall
545 oxidation matches the same rate as the overall growth, and the particle diameter ceases to
546 increase. After the steady state is reached, a hypothetical particle heavily affected by surface
547 oxidation would still be indistinguishable from a freshly nucleated particle with the currently
548 available diagnostics, or, in other words, it is not possible to find a direct link between the

549 reaction time and the particle size. Therefore, we speculate that in the premixed flames the
550 change of sign of PC1 is related to the transition from a regime dominated by the nucleation
551 of NSPs to a regime dominated by soot surface growth. The high loadings of PC1 < 0 (see
552 Fig. 7) suggest that the composition of NSPs mainly consists of small hydrocarbons having
553 molecular mass as low as m/z 90.047 ($C_7H_6^+$). Therefore, if this hypothesis is correct, by
554 following the change of sign of PC1 it is possible to mark the beginning of the sequence of
555 PAHs mainly involved in soot surface growth that eventually result in the soot deposits
556 visible even to the naked eye. The complete peak lists with corresponding attributions can be
557 found in the Supporting Information.

558 Globally, Fig. 8 shows that the same classes of molecular precursors, although spanning
559 different mass ranges, provide the building blocks of soot in different combustion
560 environments and the final product is remarkably homogeneous from a statistical point of
561 view (PCA scores). The molecular precursors involved in the formation of NSPs show a
562 remarkably similar chemical composition in both premixed flames characterized by a
563 relatively narrow distribution of small PAHs. For the diffusion flames, the pool of PAHs is
564 broadened toward higher masses. However, in the flames characterized by prominent particle
565 size growth (PRE-S, DIF-S and DIF-Q) the detected mass range is again expanded to a
566 significantly higher value in the young soot and mature soot regions. The explanation of this
567 enlargement is still not clear, and our current observations do not allow ascertaining if these
568 high mass compounds belong exclusively to the gas phase. These masses could either
569 correspond to large PAHs formed during the PAHs growth processes or to small molecular
570 clusters of medium size PAHs potentially participating to the soot nucleation. Experimentally,
571 the latter are expected to be difficult to detect by in-situ techniques, and from a fluid
572 mechanics point of view they are extremely hard to separate from the gas phase for ex-situ
573 diagnostics. However, this step of molecular clustering could be a crucial one for
574 understanding the transition from the gas to the condensed phase, and therefore each chemical
575 insight we can bring has paramount importance. To this purpose, the role of PAH
576 dimerization in the formation of NSPs is worth of particular attention being a currently much
577 debated topic [82,83,33]. The formation of Van der Waals dimers in flames is indeed
578 questionable because of the very weak bond energies, which do not theoretically enable them
579 to survive at the flame temperature. However, different authors regard as physically realistic
580 the formation of dimers in flames [5,83,84]. For instance, by using a semi-empirical
581 molecular dynamic approach, Schuetz et al. [84] showed that dimers of pyrene can be

582 stabilized by the development of free internal rotors in the colliding PAHs. More recently,
583 Kholghy et al. [83] proposed a model in which soot nucleation is not completely reversible
584 and involves a stabilization pathway of the dimers by the formation of covalent bonds through
585 a sequence of hydrogen abstraction and carbon-carbon bond formation. In this last work,
586 which is also based on data obtained from flame PRE-N, the authors conclude that only the
587 formation of dimers of small PAHs can provide soot quantities comparable to the available
588 measurements. This conclusion is therefore in excellent agreement with the results of HCA
589 and PCA in our present work that clearly highlights the prominence of small PAHs (PC1 < 0
590 in Fig. 7, m/z 93-245) in the nucleation zone before the appearance of NSPs. Hence, if dimers
591 were produced in this flame, they would necessarily originate from small PAHs as suggested
592 by our treatment. However, more efforts are still to be made to lead to the precise
593 identification of these species.

594 **3.4. Oxygen-containing hydrocarbons**

595 The mass defect analysis allows attributing a $C_mH_n^+$ molecular formula with incertitude
596 below 5 ppm to around half the total number of detected peaks. The remaining peaks are
597 assigned to OCHs based on their low mass defect that places them below the pericondensed
598 PAH limit in the mass defect plot in Fig. 4b, and based on their isotopic patterns that
599 systematically rule out low H/C fragment ions. A molecular formula $C_mH_nO_p^+$ is not
600 attributed to the individual peaks for the following reasons. Contrary to $C_mH_n^+$ ions, the peaks
601 attributed to OCHs are often asymmetrical, suggesting that more than one ion contributes to
602 the peak structure. In turn, the incertitude on the assignment of a molecular formula can be as
603 high as 15 ppm. In many cases the mass resolution is not deemed sufficient for attempting a
604 full peak deconvolution, and therefore only the accurate mass of the mode is selected for the
605 mass defect analysis. Even in the most favorable cases of well resolved and symmetrical
606 peaks, univocally attributing a $C_mH_nO_p^+$ molecular formula is not always possible with the
607 available resolving power. For instance, $C_{m-4}H_nO_3^+$ and $C_{m-7}H_{n+4}O_5^+$ require mass resolution
608 as high as 25000 and 70000, respectively, to be resolved from $C_mH_n^+$ at m/z 400.

609 As shown in the loading plots in Fig. 7c and d, OCHs (red data) are mostly found
610 associated to PC1 > 0 and PC2 < 0, and correspond to soot deposits and low HAB samples
611 from the diffusion flames as already discussed above. However, their loadings in PC2 < 0 are
612 small enough that they do not contribute significantly to the (unknown) phenomenon

613 described by PC2. In general, OCHs closely follow the behavior of PAHs but are
614 characterized by much lower ion counts in all samples and in particular in condensable gas.
615 Premixed and diffusion flames once again behave differently. In the premixed flames, OCHs
616 are mostly associated to the soot growth but the nucleation of NSPs occurs at lower HAB and
617 only involves the smaller PAHs identified in PC1 < 0. On the other hand, in the diffusion
618 flames a large amount of OCHs is found already in the gas phase before soot nucleation as
619 well as associated to NSPs. These findings are consistent with the works of Cain et al. [9] and
620 Commodo et al. [85] where it is shown that NSPs in diffusion flames contain large amounts of
621 oxygen.

622 The origin of OCHs is still being debated [34,35,9,85]. Although some works suggest that
623 data obtained with ex-situ techniques are subject to post-sampling oxidation [9], a recent
624 study points to the marginal role of the oxidation during sampling compared to the
625 combustion process [86]. In addition, both simulations [28,33] and experiments [34,85] show
626 that high mass OCHs potentially play an important role on soot nucleation. However, even if
627 the presence of OCHs represented evidence of post-sampling surface oxidation, a recent study
628 proves that OCHs are less likely to condense on soot particles [33] than PAHs, and therefore
629 those found on soot are likely to have taken part to soot formation at some point.

630 **4. Summary and conclusions**

631 Detailed information on the chemistry of nascent soot particles (NSPs) is expected to
632 provide clues on the soot formation and growth reaction pathways. The structure of many
633 laboratory flames is nowadays well understood, and this knowledge makes them very
634 desirable for both experimentalists and modelers aiming to investigate fundamental processes.
635 Herein, we discuss the data obtained from the secondary ion mass spectrometry (SIMS)
636 analysis of samples extracted from four different laboratory flames, two low-pressure
637 premixed and two atmospheric diffusion methane flames. The premixed flames are stabilized
638 in conditions that result in the soot nucleation beginning at the same reaction time, or
639 equivalently at the same height above the burner (HAB). However, in the premixed sooting
640 flame (PRE-S) soot primary particles are formed at short reaction time, while in the premixed
641 low-pressure nucleation flame (PRE-N) the equivalence ratio is chosen so that NSPs nucleate
642 all along the flame without growing in size [8,49]. To complete the set of investigated flames,
643 a sooting diffusion flame (DIF-S) and a diffusion flame quenched with argon (DIF-Q) are

644 stabilized in similar aerodynamic conditions. In contrast to the previous case, in which soot
645 and molecular precursors coexist all along the reaction coordinate, the laser induced
646 incandescence/fluorescence (LII/LIF) mapping of the diffusion flames shows a net
647 stratification of the formation regions of soot and molecular precursors that can be probed
648 separately. Flames PRE-N, PRE-S [8] and DIF-Q [53,54] were already subject to ex-situ mass
649 spectrometry investigations in the past. The much larger database of collected samples and the
650 higher mass resolution enable here the use of an improved data reduction protocol based on
651 multivariate analysis for the data mining and interpretation.

652 A database containing 152 samples is first analyzed to assess how the flame chemistry
653 influences the structure of the mass spectra. Hierarchical cluster analysis (HCA) and principal
654 component analysis (PCA) are used to classify the samples and find correspondences between
655 sample populations. PCA shows the changes in the total variance of a group of observables
656 (the samples) calculated from a set of variables (the peak ion counts). The loadings plots
657 identify the variables that have the largest effect on each principal component. Therefore, if a
658 principal component can be associated to a physical phenomenon, then PCA suggests a set of
659 variables this phenomenon depends on. This additional information is provided by LII/LIF
660 that maps the formation regions of soot and molecular precursors, and by the presence of
661 visible soot deposits on the sample surface.

662 The presence in the mass spectra of a sequence of high mass species is well represented
663 by the first principal component (PC1, 52.6% of the total variance explained). PC1 is
664 characterized by a rather sharp change of sign at m/z 165–245. Globally, samples rich in high
665 mass species feature high scores in $PC1 > 0$ and correspond to strong LII signals and the
666 formation of visible soot deposits. Conversely, samples poor in high mass species feature high
667 scores in $PC1 < 0$ and lack of LII signal or visible soot deposits. Flame PRE-N is a notable
668 exception as it features high scores in $PC1 < 0$ that are representative of the gas phase, but at
669 the same time the detection of LII signal shows that NSPs nucleate. In the diffusion flames,
670 large masses are detected at low HAB before the soot formation region identified by LII. This
671 behavior strongly implies a correlation of PC1 with the presence of NSPs in a steady state
672 ($PC1 < 0$) and with the coagulation and coalescence typical of growing soot particles and the
673 nucleation in the diffusion flames ($PC1 > 0$). In particular, the change of sign of PC1 can be
674 used to distinguish two different regimes of soot nucleation, and leads to the definition of two
675 mass lists compatible with the formation of NSPs in the investigated premixed and diffusion

676 flames. In conclusion, the presence of large molecules in the gas phase is neither a necessary
677 condition (NSPs nucleate from low mass PAHs in flame PRE-N) nor a sufficient condition
678 (large PAHs are detected in the gas phase in the absence of soot in flames DIF-S and DIF-Q)
679 for soot nucleation.

680 It was not possible to clearly associate a physical phenomenon to the second principal
681 component (PC2, 23.5% of the total variance explained).

682 On a molecular level, polycyclic aromatic hydrocarbons (PAHs) and oxygen-containing
683 hydrocarbons (OCHs) are identified by mass defect analysis and correlated to specific
684 loadings, and thus indirectly to specific soot nucleation conditions. PAHs dominate the mass
685 spectra, although a large array of OCHs is also detected in agreement with theoretical
686 calculations and predictions of modeling from the literature. The existence of a large number
687 of compounds containing an odd number of carbon atoms gives indirect evidence of the
688 importance of non-benzenoid or substituted PAHs in the nucleation and growth of NSPs. In
689 particular, many strong signals attributed to PAHs are consistent with 5-member rings that
690 further stress their importance in soot formation and growth [7]. Comparison of the data to
691 kinetic modeling shows that in the growth of both molecular precursors and compounds
692 adsorbed on soot, compact PAHs are preferred over open structures. The comparison of soot
693 sampled from different flames shows that the molecular compounds involved in soot
694 nucleation and growth, when classified according to their H/C ratio, all lie clustered around or
695 slightly above the curve representing the maximally condensed aromatics. The excellent
696 agreement with the predictions of kinetic modeling of D'Anna et al. [50] suggests a similarity
697 in behavior that can be explained by a common origin for instance. However, the
698 hydrocarbons involved in the nucleation of NSPs in premixed and diffusion flames span
699 significantly different mass ranges, below m/z 245 in the premixed flames (left part of the
700 curve) and up to m/z 731 in the diffusion flames (right part of the curve). In the diffusion
701 flames, these large PAHs are found upstream the soot nucleation zone in the gas phase. OCHs
702 are detected in all soot samples. However, PCA shows that they are only associated to the
703 nucleation of NSPs in the diffusion flames and to the particle growth in the premixed flames
704 (PC1 > 0), while they are virtually absent from the pool of molecules associated to the
705 nucleation of NSPs in the premixed flames (PC1 < 0). This behavior is in good agreement
706 with the works of Cain et al. [9] and Commodo et al. [85], and further stresses the differences
707 in the nucleation of NSPs in premixed and diffusion flames. In the premixed flames small

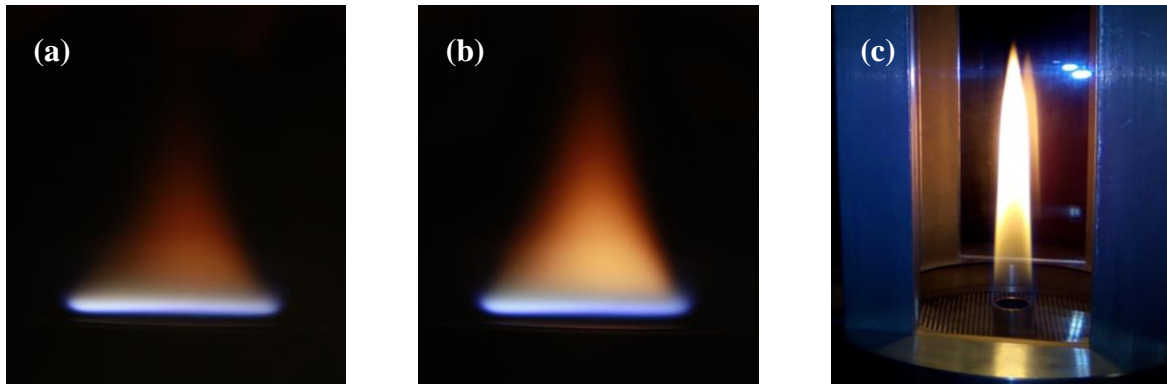
708 PAHs are sufficient to nucleate NSPs, while in the diffusion flame large amount of OCHs are
709 found from the very early steps of NSP nucleation.

710 In conclusion, large PAHs and OCHs are not required to nucleate soot. This effect is very
711 evident in at least one premixed flame (PRE-N), in which the formation of condensed phase
712 NSPs involves only PAHs having mass smaller than 400-450 u. Whether the dimer hypothesis
713 is correct, the PAHs involved in the process have mass below 200-225 u, much smaller than
714 expected from thermodynamics-based calculations to further support the idea that soot
715 formation cannot be a thermodynamically controlled process.

716 **5. Acknowledgments**

717 This work was supported by the Agence Nationale de la Recherche through the LABEX
718 CAPP (ANR-11-LABX-0005), the Ministry of Higher Education and Research,
719 Hauts-de-France Regional Council and European Regional Development Fund (ERDF)
720 through the Contrat de Projets Etat-Region (CPER CLIMIBIO), the H2020 project Portable
721 Nano Particle Emission Measurement System (PEMs4Nano, Grant Agreement no. 724145).

722



723 Fig. 1. Investigated flames. (a) Flame PRE-N and (b) flame PRE-S inside the low pressure vessel. (c) Flame DIF-S
 724 surrounded by a quartz windowed chimney [45]. During the soot sampling procedure one of the windows is removed
 725 for the sampling probe insertion. Flame DIF-Q is very similar to flame DIF-S, and therefore is not shown in the picture.

726

Flame	$Q_{\text{tot}} / \text{L min}^{-1}$	x_{methane}	x_{oxygen}	x_{nitrogen}
PRE-N	3.96	0.425	0.435	0.140
PRE-S	3.96	0.462	0.398	0.140

727 Table 1. Laminar premixed flames experimental conditions. Q_{tot} is the total flow, x_{methane} , x_{oxygen} and x_{nitrogen} the gas
 728 volume fractions. Both flames are stabilized at $p = 267 \pm 1$ mbar.

729

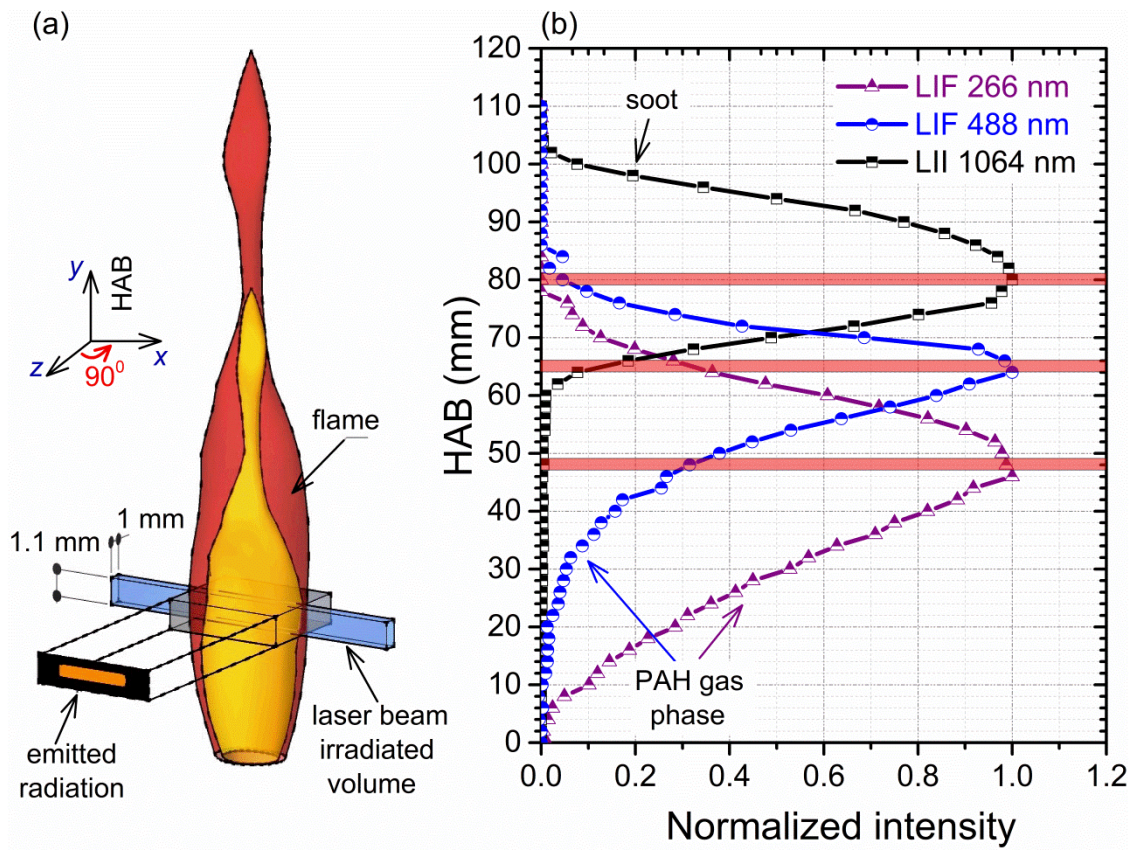
Flame	$Q_{\text{fuel}} / \text{L min}^{-1}$	$Q_{\text{dil}} / \text{L min}^{-1}$	$Q_{\text{shield}} / \text{L min}^{-1}$	h / mm
DIF-S	0.470	/	87	115
DIF-Q	0.425	0.335	76	70

730 Table 2. Laminar diffusion flames experimental conditions. Q_{fuel} is the methane flow, Q_{dil} is the dilution argon flow
 731 premixed to the methane flow, Q_{shield} is the air shield flow and h the flame visible height measured from the injector
 732 exit plane to the tip of the flame.

733

734

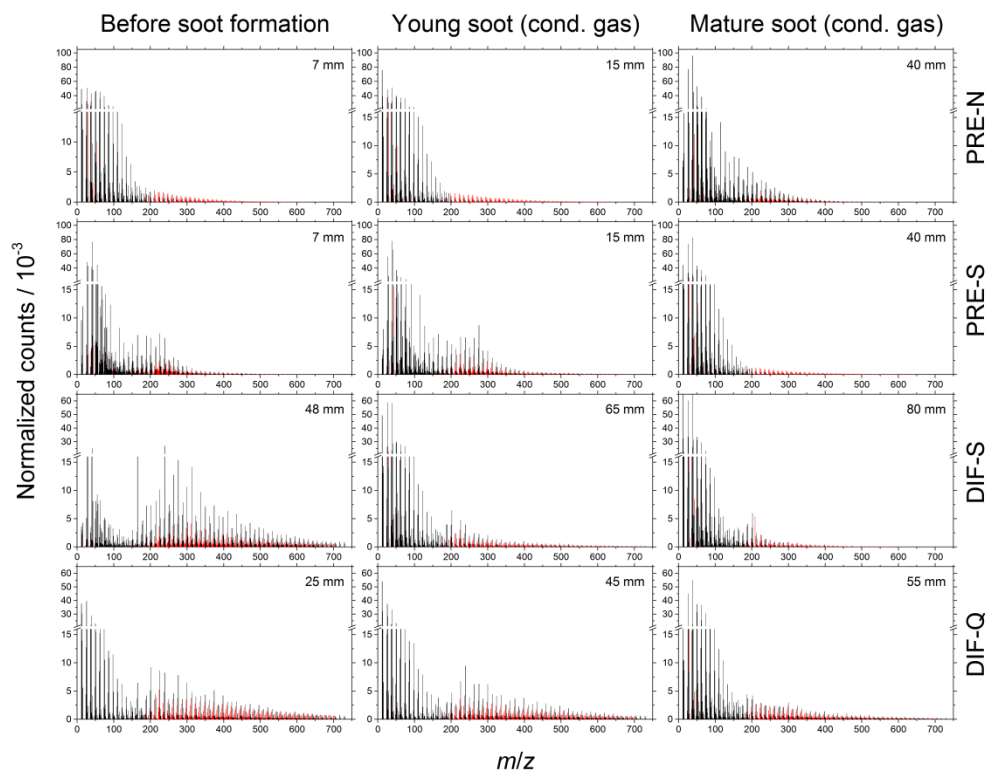
735



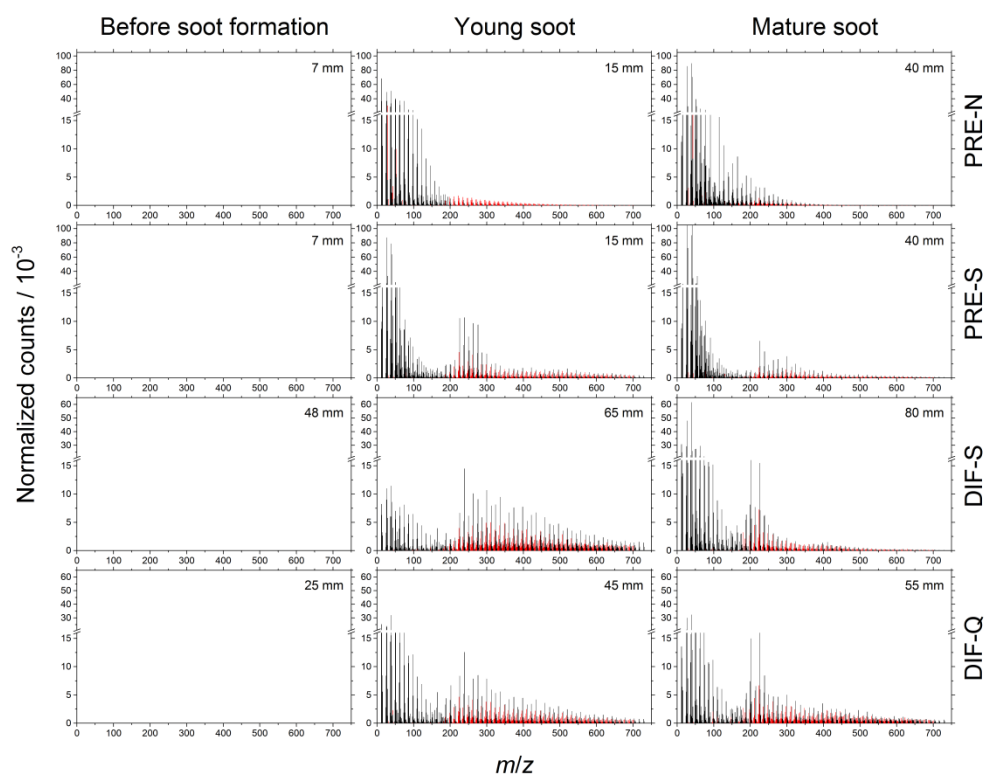
736

737 Fig. 2. DIF-S flame. (a) sketch of the LII/LIF working principle: the flame axis is irradiated with a top hat laser beam
 738 profile and the emitted radiation is collected at 90° incidence. The emission is collected from a 2 mm deep region on
 739 the centerline of the flame. (b) LII/LIF signal against HAB with highlighted sampling locations.

740

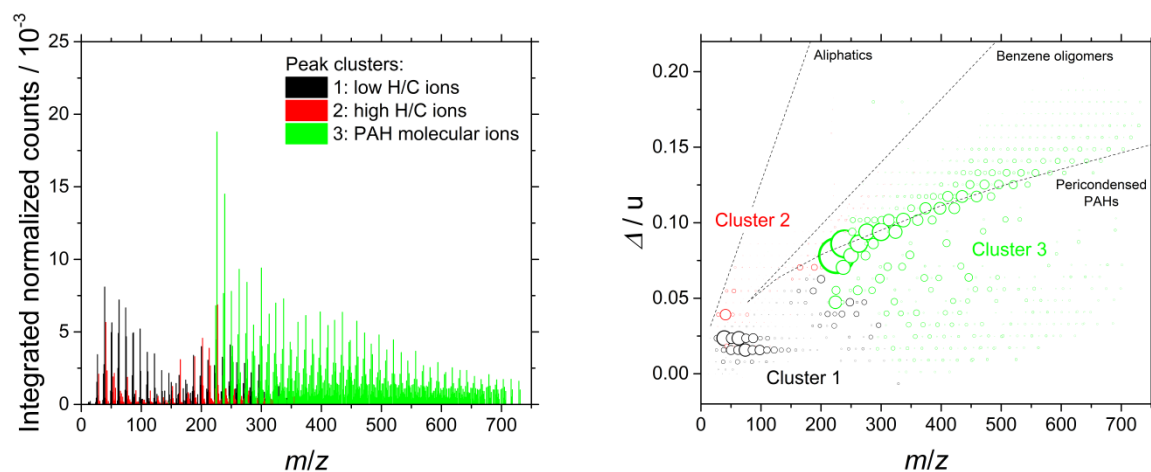


741



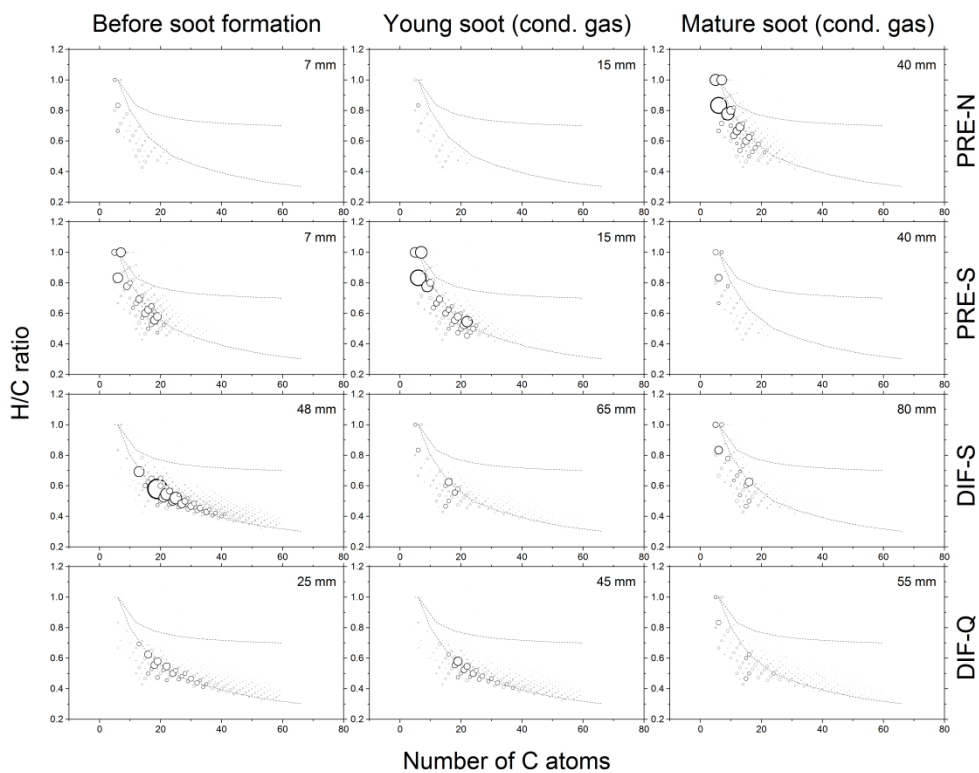
742

743 Fig. 3. Mass spectra obtained from the four investigated flames. Each column represents a flame region, from before
 744 soot nucleation (left column), to the beginning of the soot nucleation zone (middle column) and up to the mature soot
 745 region (right column). Mass spectra of condensable gas and soot are shown in the top and bottom panel, respectively.
 746 The intensity count is normalized to the partial ion count calculated from the peak list after background removal.
 747 Black and red signals represent hydrocarbons and oxygen-containing hydrocarbons, respectively.

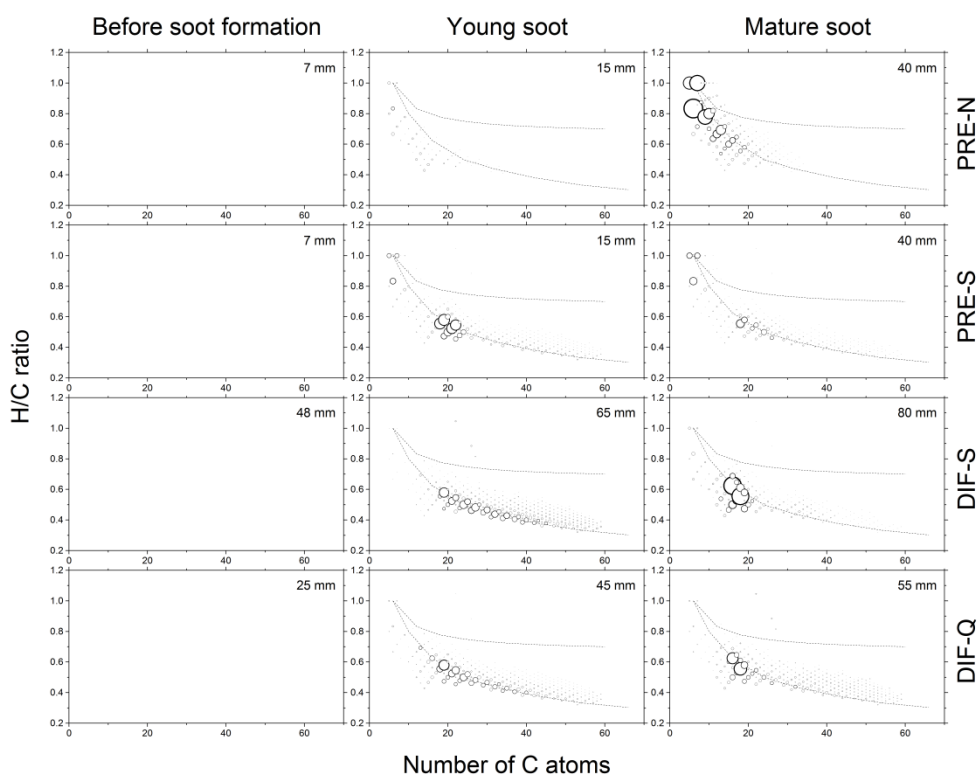


748 Fig. 4. (a) Example of HCA classification applied to one mass spectrum (flame DIF-S, 65 mm HAB), and (b) to the
 749 corresponding mass defect plot. Three patterns are identified by HCA: low H/C ions (black data) are mainly attributed
 750 to fragment ions, high H/C ions (red data) to unsaturated hydrocarbons and low-mass PAHs, and high-mass ions
 751 (green data) to PAHs and OCHs. The dot size in (b) is proportional to the integrated area of the selected peaks. The
 752 dashed lines represent the limits of aliphatic, benzene oligomers and pericondensed PAHs.

753

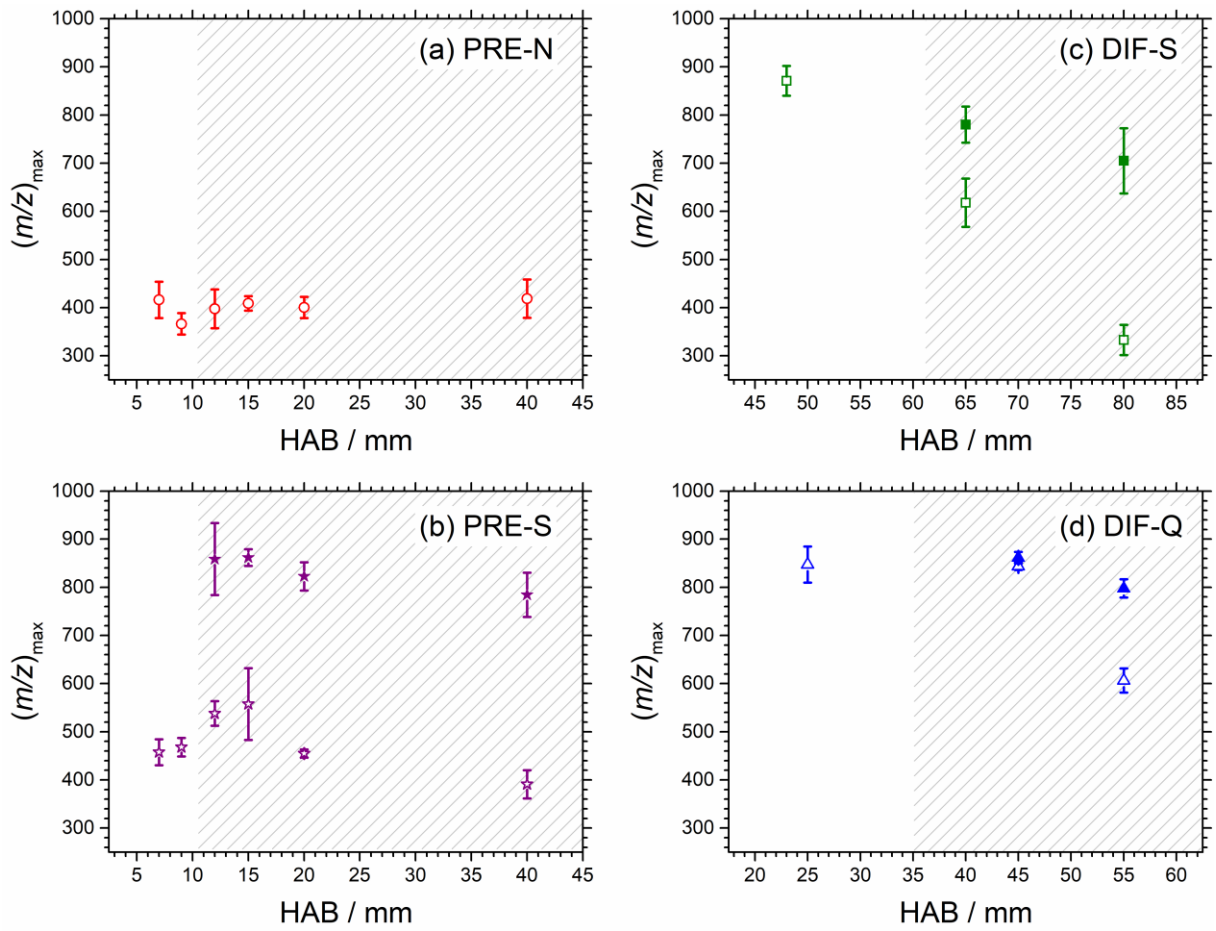


754



755

756 Fig. 5. n/m vs. m/z diagrams. Only $C_mH_n^+$ ions are plotted. Similarly to Fig. 3, rows represent different flames and
 757 columns represent different flame regions. Data obtained from the condensable gas and soot are shown in the top and
 758 bottom panel, respectively. The black dashed lines represent the limits of benzene oligomers (top line, high n/m) and
 759 pericondensed PAHs (bottom line, low n/m) from D'Anna et al. [50].



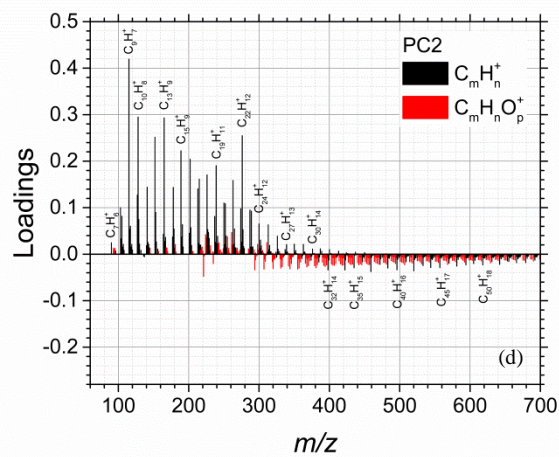
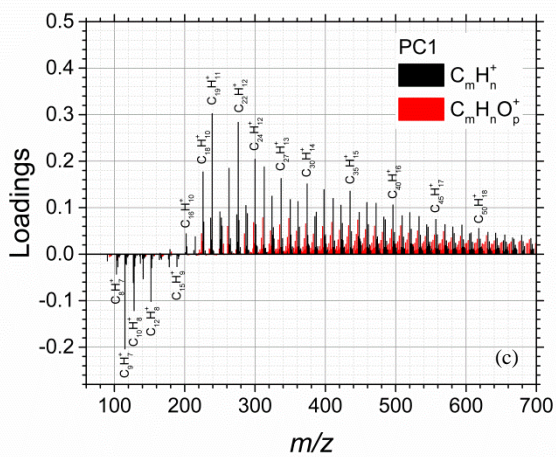
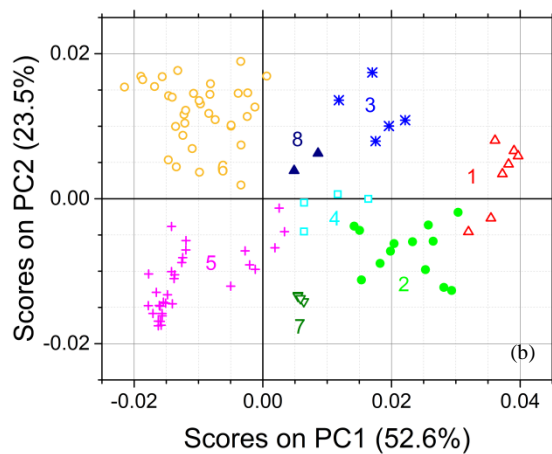
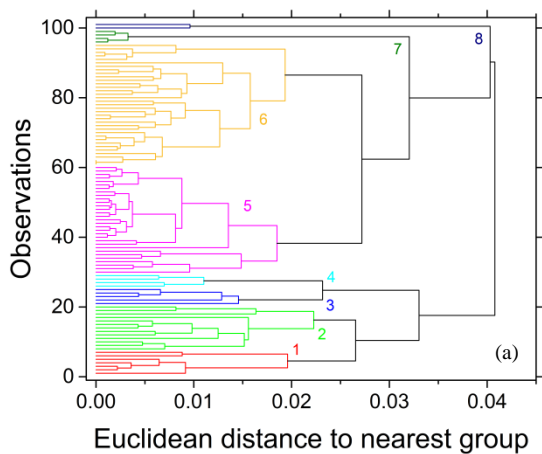
760

761

762

Fig. 6. $(m/z)_{\max}$ against HAB, sorted by flames. The error bars represent the standard deviation calculated on three samples. The gray patterns mark the soot region determined by LII /LIF measurements.

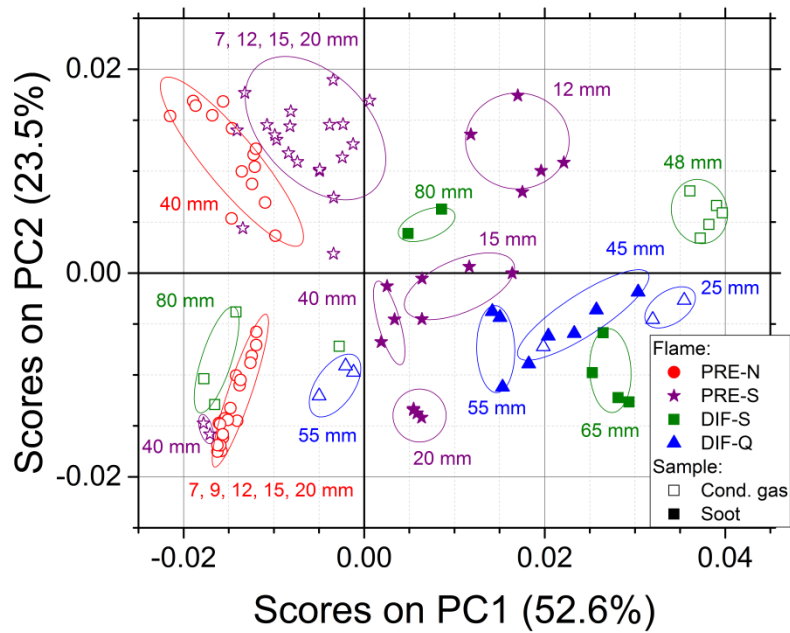
763



764 Fig. 7. Samples classification obtained by HCA and PCA. In the top row, the HCA dendrogram (a) and the PC2 vs. PC1
 765 score plot (b) are compared. The colors and cluster numbers match in the two representations. In the bottom row, the
 766 loading plots of PC1 and PC2 against m/z are shown.

Data cluster	PRE-N	PRE-S	DIF-S	DIF-Q
1	/	/	48	25
2	/	/	65*	45*,55*
3	/	12*	/	/
4	/	15*	/	/
5	7,9,12,15,20	40, 40*	80	55
6	15,40	7,9,12,15,20	/	/
7	/	20*	/	/
8	/	/	80*	/

767 Table 3. Classification of samples by HCA and PCA clusters (rows) and flames (columns). Each cell contains the
768 sampled HAB. Bold starred and normal text mark the samples obtained from the analysis of soot and the condensable
769 gas phase, respectively.



770

771 Fig. 8. PC2 vs. PC1 score plot with samples classified by flame (data point shape and color) and analysis of soot or
772 condensable gas (data point interior).

773

774 **6. References**

- 775 [1] M. Frenklach, Reaction mechanism of soot formation in flames, *Phys. Chem. Chem.*
776 *Phys.* 4 (2002) 2028–2037. doi:10.1039/B110045A.
- 777 [2] A. D’Anna, Combustion-formed nanoparticles, *Proc. Combust. Inst.* 32 (2009) 593–613.
778 doi:10.1016/j.proci.2008.09.005.
- 779 [3] H. Wang, Formation of nascent soot and other condensed-phase materials in flames,
780 *Proc. Combust. Inst.* 33 (2011) 41–67. doi:10.1016/j.proci.2010.09.009.
- 781 [4] A.E. Karataş, Ö.L. Gülder, Soot formation in high pressure laminar diffusion flames,
782 *Prog. Energy Combust. Sci.* 38 (2012) 818–845. doi:10.1016/j.pecs.2012.04.003.
- 783 [5] N.A. Eaves, S.B. Dworkin, M.J. Thomson, Assessing relative contributions of PAHs to
784 soot mass by reversible heterogeneous nucleation and condensation, *Proc. Combust.*
785 *Inst.* 36 (2017) 935–945. doi:10.1016/j.proci.2016.06.051.
- 786 [6] M. Commodo, G. De Falco, A. Bruno, C. Borriello, P. Minutolo, A. D’Anna,
787 Physicochemical evolution of nascent soot particles in a laminar premixed flame: from
788 nucleation to early growth, *Combust. Flame.* 162 (2015) 3854–3863.
789 doi:10.1016/j.combustflame.2015.07.022.
- 790 [7] K.O. Johansson, T. Dillstrom, P. Elvati, M.F. Campbell, P.E. Schrader, D.M. Popolan-
791 Vaida, N.K. Richards-Henderson, K.R. Wilson, A. Violi, H.A. Michelsen, Radical-
792 radical reactions, pyrene nucleation, and incipient soot formation in combustion, *Proc.*
793 *Combust. Inst.* 36 (2017) 799–806. doi:10.1016/j.proci.2016.07.130.
- 794 [8] P. Desgroux, A. Faccinetto, X. Mercier, T. Mouton, D. Aubagnac Karkar, A. El Bakali,
795 Comparative study of the soot formation process in a nucleation and a sooting low
796 pressure premixed methane flame, *Combust. Flame.* 184 (2017) 153–166.
797 doi:10.1016/j.combustflame.2017.05.034.
- 798 [9] J. Cain, A. Laskin, M.R. Kholghy, M.J. Thomson, H. Wang, Molecular characterization
799 of organic content of soot along the centerline of a coflow diffusion flame, *Phys. Chem.*
800 *Chem. Phys.* 16 (2014) 25862–25875. doi:10.1039/C4CP03330B.

- 801 [10] P.D. Teini, D.M.A. Karwat, A. Atreya, Observations of nascent soot: molecular
802 deposition and particle morphology, *Combust. Flame.* 158 (2011) 2045–2055.
803 doi:10.1016/j.combustflame.2011.03.005.
- 804 [11] F. Carbone, S. Moslih, A. Gomez, Probing gas-to-particle transition in a moderately
805 sooting atmospheric pressure ethylene/air laminar premixed flame. Part II: Molecular
806 clusters and nascent soot particle size distributions, *Combust. Flame.* 181 (2017) 329–
807 341. doi:10.1016/j.combustflame.2017.02.021.
- 808 [12] P. Desgroux, X. Mercier, K.A. Thomson, Study of the formation of soot and its
809 precursors in flames using optical diagnostics, *Proc. Combust. Inst.* 34 (2013) 1713–
810 1738. doi:10.1016/j.proci.2012.09.004.
- 811 [13] H.A. Michelsen, C. Schulz, G.J. Smallwood, S. Will, Laser-induced incandescence:
812 particulate diagnostics for combustion, atmospheric, and industrial applications, *Prog.*
813 *Energy Combust. Sci.* 51 (2015) 2–48. doi:10.1016/j.pecs.2015.07.001.
- 814 [14] C. Betrancourt, F. Liu, P. Desgroux, X. Mercier, A. Faccinetto, M. Salamanca, L. Ruwe,
815 K. Kohse-Höinghaus, D. Emmrich, A. Beyer, A. Gölzhäuser, T. Tritscher, Investigation
816 of the size of the incandescent incipient soot particles in premixed sooting and
817 nucleation flames of n-butane using LII, HIM, and 1 nm-SMPS, *Aerosol Sci. Technol.*
818 51 (2017) 916–935. doi:10.1080/02786826.2017.1325440.
- 819 [15] R.L. Vander Wal, A.J. Tomasek, Soot nanostructure: dependence upon synthesis
820 conditions, *Combust. Flame.* 136 (2004) 129–140.
821 doi:10.1016/j.combustflame.2003.09.008.
- 822 [16] M.R. Kholghy, A. Veshkini, M.J. Thomson, The core–shell internal nanostructure of
823 soot – A criterion to model soot maturity, *Carbon.* 100 (2016) 508–536.
824 doi:10.1016/j.carbon.2016.01.022.
- 825 [17] B. Apicella, P. Pré, M. Alfè, A. Ciajolo, V. Gargiulo, C. Russo, A. Tregrossi, D.
826 Deldique, J.N. Rouzaud, Soot nanostructure evolution in premixed flames by high
827 resolution electron transmission microscopy (HRTEM), *Proc. Combust. Inst.* 35 (2015)
828 1895–1902. doi:10.1016/j.proci.2014.06.121.
- 829 [18] S.J. Harris, I.M. Kennedy, The coagulation of soot particles with Van der Waals forces,
830 *Combust. Sci. Technol.* 59 (1988) 443–454. doi:10.1080/00102208808947110.

- 831 [19] M. Frenklach, H. Wang, Detailed modeling of soot particle nucleation and growth, *Proc.*
832 *Combust. Inst.* 23 (1990) 1559–1566. doi:10.1016/S0082-0784(06)80426-1.
- 833 [20] J.S. Lowe, J.Y.W. Lai, P. Elvati, A. Violi, Towards a predictive model for polycyclic
834 aromatic hydrocarbon dimerization propensity, *Proc. Combust. Inst.* 35 (2015) 1827–
835 1832. doi:10.1016/j.proci.2014.06.142.
- 836 [21] A. Violi, A.F. Sarofim, G.A. Voth, Kinetic Monte Carlo molecular dynamics approach
837 to model soot inception, *Combust. Sci. Technol.* 176 (2004) 991–1005.
838 doi:10.1080/00102200490428594.
- 839 [22] Q. Mao, A.C.T. van Duin, K.H. Luo, Formation of incipient soot particles from
840 polycyclic aromatic hydrocarbons: A ReaxFF molecular dynamics study, *Carbon.* 121
841 (2017) 380–388. doi:10.1016/j.carbon.2017.06.009.
- 842 [23] S.E. Stein, A. Fahr, High-temperature stabilities of hydrocarbons, *J. Phys. Chem.* 89
843 (1985) 3714–3725. doi:10.1021/j100263a027.
- 844 [24] B. Öktem, M.P. Tolocka, B. Zhao, H. Wang, M.V. Johnston, Chemical species
845 associated with the early stage of soot growth in a laminar premixed ethylene–oxygen–
846 argon flame, *Combust. Flame.* 142 (2005) 364–373.
847 doi:10.1016/j.combustflame.2005.03.016.
- 848 [25] R.A. Dobbins, R.A. Fletcher, B.A. Benner, S. Hoefft, Polycyclic aromatic hydrocarbons
849 in flames, in diesel fuels, and in diesel emissions, *Combust. Flame.* 144 (2006) 773–781.
850 doi:10.1016/j.combustflame.2005.09.008.
- 851 [26] M.M. Maricq, Physical and chemical comparison of soot in hydrocarbon and biodiesel
852 fuel diffusion flames: A study of model and commercial fuels, *Combust. Flame.* 158
853 (2011) 105–116. doi:10.1016/j.combustflame.2010.07.022.
- 854 [27] A. Faccinetto, P. Desgroux, M. Ziskind, E. Therssen, C. Focsa, High-sensitivity
855 detection of polycyclic aromatic hydrocarbons adsorbed onto soot particles using laser
856 desorption/laser ionization/time-of-flight mass spectrometry: an approach to studying the
857 soot inception process in low-pressure flames, *Combust. Flame.* 158 (2011) 227–239.
858 doi:10.1016/j.combustflame.2010.08.012.

- 859 [28] P. Elvati, A. Violi, Thermodynamics of poly-aromatic hydrocarbon clustering and the
860 effects of substituted aliphatic chains, *Proc. Combust. Inst.* 34 (2013) 1837–1843.
861 doi:10.1016/j.proci.2012.07.030.
- 862 [29] A. Raj, M. Celnik, R. Shirley, M. Sander, R. Patterson, R. West, M. Kraft, A statistical
863 approach to develop a detailed soot growth model using PAH characteristics, *Combust.*
864 *Flame.* 156 (2009) 896–913. doi:10.1016/j.combustflame.2009.01.005.
- 865 [30] H. Richter, J.B. Howard, Formation of polycyclic aromatic hydrocarbons and their
866 growth to soot—a review of chemical reaction pathways, *Prog. Energy Combust. Sci.* 26
867 (2000) 565–608. doi:10.1016/S0360-1285(00)00009-5.
- 868 [31] M.M. Maricq, An examination of soot composition in premixed hydrocarbon flames via
869 laser ablation particle mass spectrometry, *J. Aerosol Sci.* 40 (2009) 844–857.
870 doi:10.1016/j.jaerosci.2009.07.001.
- 871 [32] F. Schulz, M. Commodo, K. Kaiser, G. De Falco, P. Minutolo, G. Meyer, A. D`Anna, L.
872 Gross, Insights into incipient soot formation by atomic force microscopy, *Proc.*
873 *Combust. Inst.* (2018). doi:10.1016/j.proci.2018.06.100.
- 874 [33] P. Elvati, A. Violi, Homo-dimerization of oxygenated polycyclic aromatic hydrocarbons
875 under flame conditions, *Fuel.* 222 (2018) 307–311. doi:10.1016/j.fuel.2018.02.095.
- 876 [34] K.O. Johansson, T. Dillstrom, M. Monti, F. El Gabaly, M.F. Campbell, P.E. Schrader,
877 D.M. Popolan-Vaida, N.K. Richards-Henderson, K.R. Wilson, A. Violi, H.A. Michelsen,
878 Formation and emission of large furans and oxygenated hydrocarbons from flames, *Proc.*
879 *Natl. Acad. Sci.* 113 (2016) 8374–8379. doi:10.1073/pnas.1604772113.
- 880 [35] P. Elvati, V.T. Dillstrom, A. Violi, Oxygen driven soot formation, *Proc. Combust. Inst.*
881 36 (2017) 825–832. doi:10.1016/j.proci.2016.09.019.
- 882 [36] R.L. Vander Wal, A. Yezerets, N.W. Currier, D.H. Kim, C.M. Wang, HRTEM Study of
883 diesel soot collected from diesel particulate filters, *Carbon.* 45 (2007) 70–77.
884 doi:10.1016/j.carbon.2006.08.005.
- 885 [37] G.A. Kelesidis, E. Goudeli, S.E. Pratsinis, Morphology and mobility diameter of
886 carbonaceous aerosols during agglomeration and surface growth, *Carbon.* 121 (2017)
887 527–535. doi:10.1016/j.carbon.2017.06.004.

- 888 [38] P. Desgroux, X. Mercier, B. Lefort, R. Lemaire, E. Therssen, J.-F. Pauwels, Soot volume
889 fraction measurement in low-pressure methane flames by combining laser-induced
890 incandescence and cavity ring-down spectroscopy: Effect of pressure on soot formation,
891 *Combust. Flame.* 155 (2008) 289–301. doi:10.1016/j.combustflame.2008.05.016.
- 892 [39] J. Yon, R. Lemaire, E. Therssen, P. Desgroux, A. Coppalle, K.F. Ren, Examination of
893 wavelength dependent soot optical properties of diesel and diesel/rapeseed methyl ester
894 mixture by extinction spectra analysis and LII measurements, *Appl. Phys. B.* 104 (2011)
895 253–271. doi:10.1007/s00340-011-4416-4.
- 896 [40] A.D. Abid, N. Heinz, E.D. Tolmachoff, D.J. Phares, C.S. Campbell, H. Wang, On
897 evolution of particle size distribution functions of incipient soot in premixed ethylene-
898 oxygen-argon flames, *Combust. Flame.* 154 (2008) 775–788.
899 doi:10.1016/j.combustflame.2008.06.009.
- 900 [41] M. Schenk, S. Lieb, H. Vieker, A. Beyer, A. Gölzhäuser, H. Wang, K. Kohse-
901 Höinghaus, Imaging nanocarbon materials: soot particles in flames are not structurally
902 homogeneous, *ChemPhysChem.* 14 (2013) 3248–3254. doi:10.1002/cphc.201300581.
- 903 [42] H.-H. Grotheer, H. Pokorny, K.-L. Barth, M. Thierley, M. Aigner, Mass spectrometry up
904 to 1 million mass units for the simultaneous detection of primary soot and of soot
905 precursors (nanoparticles) in flames, *Chemosphere.* 57 (2004) 1335–1342.
906 doi:10.1016/j.chemosphere.2004.08.054.
- 907 [43] B. Apicella, A. Carpentieri, M. Alfè, R. Barbella, A. Tregrossi, P. Pucci, A. Ciajolo,
908 Mass spectrometric analysis of large PAH in a fuel-rich ethylene flame, *Proc. Combust.*
909 *Inst.* 31 (2007) 547–553. doi:10.1016/j.proci.2006.08.014.
- 910 [44] R.A. Dobbins, R.A. Fletcher, H.-C. Chang, The evolution of soot precursor particles in a
911 diffusion flame, *Combust. Flame.* 115 (1998) 285–298. doi:10.1016/S0010-
912 2180(98)00010-8.
- 913 [45] C. Irimiea, A. Faccinetto, Y. Carpentier, I.-K. Ortega, N. Nuns, E. Therssen, P.
914 Desgroux, C. Focsa, A comprehensive protocol for chemical analysis of flame
915 combustion emissions by secondary ion mass spectrometry, *Rapid Commun. Mass*
916 *Spectrom.* 32 (2018) 1015–1025. doi:10.1002/rcm.8133.

- 917 [46] R. Bro, A.K. Smilde, Principal component analysis, *Anal. Methods*. 6 (2014) 2812–
918 2831. doi:10.1039/C3AY41907J.
- 919 [47] I.T. Jolliffe, J. Cadima, Principal component analysis: a review and recent developments,
920 *Philos. Transact. A Math. Phys. Eng. Sci.* 374 (2016) 20150202.
921 doi:10.1098/rsta.2015.0202.
- 922 [48] T. Mouton, X. Mercier, M. Wartel, N. Lamoureux, P. Desgroux, Laser-induced
923 incandescence technique to identify soot nucleation and very small particles in low-
924 pressure methane flames, *Appl. Phys. B*. 112 (2013) 369–379. doi:10.1007/s00340-013-
925 5446-x.
- 926 [49] D. Aubagnac-Karkar, A. El Bakali, P. Desgroux, Soot particles inception and PAH
927 condensation modelling applied in a soot model utilizing a sectional method, *Combust.*
928 *Flame*. 189 (2018) 190–206. doi:10.1016/j.combustflame.2017.10.027.
- 929 [50] A. D’Anna, M. Sirignano, J. Kent, A model of particle nucleation in premixed ethylene
930 flames, *Combust. Flame*. 157 (2010) 2106–2115.
931 doi:10.1016/j.combustflame.2010.04.019.
- 932 [51] H. Bladh, N.-E. Olofsson, T. Mouton, J. Simonsson, X. Mercier, A. Faccinetto, P.-E.
933 Bengtsson, P. Desgroux, Probing the smallest soot particles in low-sooting premixed
934 flames using laser-induced incandescence, *Proc. Combust. Inst.* 35 (2015) 1843–1850.
935 doi:10.1016/j.proci.2014.06.001.
- 936 [52] J.C. Biordi, C.P. Lazzara, J.F. Papp, Molecular beam mass spectrometry applied to
937 determining the kinetics of reactions in flames. I. Empirical characterization of flame
938 perturbation by molecular beam sampling probes, *Combust. Flame*. 23 (1974) 73–82.
939 doi:10.1016/S0010-2180(74)80028-3.
- 940 [53] H. Hepp, K. Siegmann, Mapping of soot particles in a weakly sooting diffusion flame by
941 aerosol techniques, *Combust. Flame*. 115 (1998) 275–283. doi:10.1016/S0010-
942 2180(97)00346-5.
- 943 [54] K. Siegmann, K. Sattler, H.C. Siegmann, Clustering at high temperatures: carbon
944 formation in combustion, *J. Electron Spectrosc. Relat. Phenom.* 126 (2002) 191–202.
945 doi:10.1016/S0368-2048(02)00152-4.

- 946 [55] H.A. Michelsen, Probing soot formation, chemical and physical evolution, and
947 oxidation: A review of in situ diagnostic techniques and needs, *Proc. Combust. Inst.* 36
948 (2017) 717–735. doi:10.1016/j.proci.2016.08.027.
- 949 [56] C. Schoemaeker Moreau, E. Therssen, X. Mercier, J.-F. Pauwels, P. Desgroux, Two-
950 color laser-induced incandescence and cavity ring-down spectroscopy for sensitive and
951 quantitative imaging of soot and PAHs in flames, *Appl. Phys. B.* 78 (2004) 485–492.
952 doi:10.1007/s00340-003-1370-9.
- 953 [57] S. Bejaoui, R. Lemaire, E. Therssen, Analysis of laser-induced fluorescence spectra
954 obtained in spray flames of diesel and rapeseed methyl ester using the multiple-
955 excitation wavelength laser-induced incandescence technique with IR, UV, and visible
956 excitations, *Combust. Sci. Technol.* 187 (2015) 906–924.
957 doi:10.1080/00102202.2014.973949.
- 958 [58] M. Wartel, J.-F. Pauwels, P. Desgroux, X. Mercier, Pyrene measurements in sooting low
959 pressure methane flames by jet-cooled laser-induced fluorescence, *J. Phys. Chem. A.*
960 115 (2011) 14153–14162. doi:10.1021/jp206970t.
- 961 [59] H.J. Heger, R. Zimmermann, R. Dorfner, M. Beckmann, H. Griebel, A. Kettrup, U.
962 Boesl, On-line emission analysis of polycyclic aromatic hydrocarbons down to pptv
963 concentration levels in the flue gas of an incineration pilot plant with a mobile
964 resonance-enhanced multiphoton ionization time-of-flight mass spectrometer, *Anal.*
965 *Chem.* 71 (1999) 46–57. doi:10.1021/ac980611y.
- 966 [60] A.C. Aiken, P.F. DeCarlo, J.L. Jimenez, Elemental analysis of organic species with
967 electron ionization high-resolution mass spectrometry, *Anal. Chem.* 79 (2007) 8350–
968 8358. doi:10.1021/ac071150w.
- 969 [61] L.M. Russell, R. Bahadur, L.N. Hawkins, J. Allan, D. Baumgardner, P.K. Quinn, T.S.
970 Bates, Organic aerosol characterization by complementary measurements of chemical
971 bonds and molecular fragments, *Atmos. Environ.* 43 (2009) 6100–6105.
972 doi:10.1016/j.atmosenv.2009.09.036.
- 973 [62] D.S. Liscinsky, Z. Yu, B. True, J. Peck, A.C. Jennings, H.-W. Wong, J. Franklin, S.C.
974 Herndon, R.C. Mlake-Lye, Measurement of naphthalene uptake by combustion soot
975 particles, *Environ. Sci. Technol.* 47 (2013) 4875–4881. doi:10.1021/es304912d.

- 976 [63] M.T. Timko, S.E. Albo, T.B. Onasch, E.C. Fortner, Z. Yu, R.C. Miake-Lye, M.R.
977 Canagaratna, N.L. Ng, D.R. Worsnop, Composition and sources of the organic particle
978 emissions from aircraft engines, *Aerosol Sci. Technol.* 48 (2014) 61–73.
979 doi:10.1080/02786826.2013.857758.
- 980 [64] K.O. Johansson, J. Zádor, P. Elvati, M.F. Campbell, P.E. Schrader, N.K. Richards-
981 Henderson, K.R. Wilson, A. Violi, H.A. Michelsen, Critical assessment of
982 photoionization efficiency measurements for characterization of soot-precursor species,
983 *J. Phys. Chem. A.* 121 (2017) 4475–4485. doi:10.1021/acs.jpca.7b02992.
- 984 [65] M.D. Hays, R.J. Lavrich, Developments in direct thermal extraction gas
985 chromatography-mass spectrometry of fine aerosols, *Trend Anal Chem.* 26 (2007) 88–
986 102.
- 987 [66] J. Gil-Moltó, M. Varea, N. Galindo, J. Crespo, Application of an automatic thermal
988 desorption-gas chromatography-mass spectrometry system for the analysis of polycyclic
989 aromatic hydrocarbons in airborne particulate matter, *J. Chromatogr. A.* 1216 (2009)
990 1285–1289. doi:10.1016/j.chroma.2008.12.080.
- 991 [67] C. Mihesan, M. Ziskind, E. Therssen, P. Desgroux, C. Focsa, IR laser resonant
992 desorption of polycyclic aromatic hydrocarbons, *Chem. Phys. Lett.* 423 (2006) 407–412.
993 doi:10.1016/j.cplett.2006.04.032.
- 994 [68] O.P. Haefliger, R. Zenobi, New sample preparation for quantitative laser desorption
995 mass spectrometry and optical spectroscopy, *Rev. Sci. Instrum.* 69 (1998) 1828–1832.
- 996 [69] J.W.G. Bentz, J. Goschnick, J. Schuricht, H.J. Ache, J. Zehnpfennig, A. Benninghoven,
997 Analysis and classification of individual outdoor aerosol particles with SIMS time-of-
998 flight mass spectrometry, *Fresenius J. Anal. Chem.* 353 (1995) 603–608.
999 doi:10.1007/BF00321333.
- 1000 [70] O.B. Popovicheva, C. Irimiea, Y. Carpentier, I.K. Ortega, E.D. Kireeva, N.K. Shonija, J.
1001 Schwarz, M. Vojtíšek-Lom, C. Focsa, Chemical composition of diesel/biodiesel
1002 particulate exhaust by FTIR spectroscopy and mass spectrometry: impact of fuel and
1003 driving cycle, *Aerosol Air Qual. Res.* 17 (2017) 1717–1734.
1004 doi:10.4209/aaqr.2017.04.0127.

- 1005 [71] T. Stephan, E.K. Jessberger, C.H. Heiss, D. Rost, TOF-SIMS analysis of polycyclic
1006 aromatic hydrocarbons in Allan Hills 84001, *Meteorit. Planet. Sci.* 38 (2003) 109–116.
1007 doi:10.1111/j.1945-5100.2003.tb01049.x.
- 1008 [72] R.E. Peterson, B.J. Tyler, Analysis of organic and inorganic species on the surface of
1009 atmospheric aerosol using time-of-flight secondary ion mass spectrometry (TOF-SIMS),
1010 *Atmos. Environ.* 36 (2002) 6041–6049. doi:10.1016/S1352-2310(02)00686-6.
- 1011 [73] L. Pei, G. Jiang, B.J. Tyler, L.L. Baxter, M.R. Linford, Time-of-flight secondary ion
1012 mass spectrometry of a range of coal samples: A chemometrics (PCA, cluster, and PLS)
1013 analysis, *Energy Fuels.* 22 (2008) 1059–1072. doi:10.1021/ef7003199.
- 1014 [74] P. Reitz, S.R. Zorn, S.H. Trimborn, A.M. Trimborn, A new, powerful technique to
1015 analyze single particle aerosol mass spectra using a combination of OPTICS and the
1016 fuzzy c-means algorithm, *J. Aerosol Sci.* 98 (2016) 1–14.
1017 doi:10.1016/j.jaerosci.2016.04.003.
- 1018 [75] H. Abdi, L. Williams, Principal component analysis, *Wiley Interdiscip Rev Comput Stat.*
1019 2 (2010) 433–459. doi:10.1002/wics.101.
- 1020 [76] R. Baigorri, A.M. Zamarreño, M. Fuentes, G. González-Gaitano, J.M. García-Mina, G.
1021 Almendros, F.J. González-Vila, Multivariate statistical analysis of mass spectra as a tool
1022 for the classification of the main humic substances according to their structural and
1023 conformational features, *J. Agric. Food Chem.* 56 (2008) 5480–5487.
1024 doi:10.1021/jf800507u.
- 1025 [77] O.P. Haefliger, R. Zenobi, Laser mass spectrometric analysis of polycyclic aromatic
1026 hydrocarbons with wide wavelength range laser multiphoton ionization spectroscopy,
1027 *Anal. Chem.* 70 (1998) 2660–2665. doi:10.1021/ac971264f.
- 1028 [78] L. Sleno, The use of mass defect in modern mass spectrometry, *J. Mass Spectrom.* 47
1029 (2012) 226–236. doi:10.1002/jms.2978.
- 1030 [79] A. Keller, R. Kovacs, K.-H. Homann, Large molecules, ions, radicals and small soot
1031 particles in fuel-rich hydrocarbon flames. Part IV. Large polycyclic aromatic
1032 hydrocarbons and their radicals in a fuel-rich benzene-oxygen flame, *Phys. Chem.*
1033 *Chem. Phys.* 2 (2000) 1667–1675. doi:10.1039/A908190I.

- 1034 [80] D. Chen, Z. Zainuddin, E. Yapp, J. Akroyd, S. Mosbach, M. Kraft, A fully coupled
1035 simulation of PAH and soot growth with a population balance model, *Proc. Combust.*
1036 *Inst.* 34 (2013) 1827–1835. doi:10.1016/j.proci.2012.06.089.
- 1037 [81] K.O. Johansson, M.P. Head-Gordon, P.E. Schrader, K.R. Wilson, H.A. Michelsen,
1038 Resonance-stabilized hydrocarbon-radical chain reactions may explain soot inception
1039 and growth, *Science*. 361 (2018) 997. doi:10.1126/science.aat3417.
- 1040 [82] H.-B. Zhang, X. You, H. Wang, C.K. Law, Dimerization of polycyclic aromatic
1041 hydrocarbons in soot nucleation, *J. Phys. Chem. A*. 118 (2014) 1287–1292.
1042 doi:10.1021/jp411806q.
- 1043 [83] M.R. Kholghy, G.A. Kelesidis, S.E. Pratsinis, Reactive polycyclic aromatic hydrocarbon
1044 dimerization drives soot nucleation, *Phys. Chem. Chem. Phys.* 20 (2018) 10926–10938.
1045 doi:10.1039/C7CP07803J.
- 1046 [84] C.A. Schuetz, M. Frenklach, Nucleation of soot: Molecular dynamics simulations of
1047 pyrene dimerization, *Proc. Combust. Inst.* 29 (2002) 2307–2314. doi:10.1016/S1540-
1048 7489(02)80281-4.
- 1049 [85] M. Commodo, A. D’Anna, G. De Falco, R. Larciprete, P. Minutolo, Illuminating the
1050 earliest stages of the soot formation by photoemission and Raman spectroscopy,
1051 *Combust. Flame*. 181 (2017) 188–197. doi:10.1016/j.combustflame.2017.03.020.
- 1052 [86] F.-X. Ouf, P. Parent, C. Laffon, I. Marhaba, D. Ferry, B. Marcillaud, E. Antonsson, S.
1053 Benkoula, X.-J. Liu, C. Nicolas, E. Robert, M. Patanen, F.-A. Barreda, O. Sublemontier,
1054 A. Coppalle, J. Yon, F. Miserque, T. Mostefaoui, T.Z. Regier, J.-B.A. Mitchell, C.
1055 Miron, First in-flight synchrotron X-ray absorption and photoemission study of carbon
1056 soot nanoparticles, *Sci. Rep.* 6 (2016) 36495. doi:10.1038/srep36495.

1058 1. SI. Definition of terms used in mass spectrometry

1059 This section contains the IUPAC definitions of some terms related to mass spectrometry
1060 and used in the paper [87].

- 1061 • *Accurate mass*. Experimentally determined mass of an ion of known charge. Can
1062 be used to determine elemental composition to within limits defined by both the
1063 accuracy and precision of the measurement.
- 1064 • *Exact mass*. Calculated mass of an ion or molecule with specified isotopic
1065 composition.
- 1066 • *Mass calibration*. Means of determining m/z values of ions from experimentally
1067 detected signals using a theoretical or empirical relational equation. Most
1068 commonly, this is accomplished using a computer-based data system and a
1069 calibration file obtained from a mass spectrum of a compound that produces ions
1070 of known m/z values.
- 1071 • *Mass defect*. Difference between the nominal mass and the monoisotopic mass of
1072 an atom, molecule, or ion. Mass defect can be a positive or negative value
1073 dependent upon the elemental composition.
- 1074 • *Monoisotopic mass*. Exact mass of an ion or molecule calculated using the mass of
1075 the most abundant isotope of each element.
- 1076 • m/z . Abbreviation representing the dimensionless quantity formed by dividing the
1077 ratio of the mass of an ion to the unified atomic mass unit, by its charge number
1078 (regardless of sign). The abbreviation is written in italicized lowercase letters with
1079 no spaces. m/z is recommended as an abbreviation to represent the dimensionless
1080 quantity that is used almost universally as the independent variable in a mass
1081 spectrum. The abbreviation m/z should not be used as a variable in a mathematical
1082 equation. Instead, the variables m (in kg) and q (in C) should be used to denote
1083 mass and charge
- 1084 • *Nominal mass*. Mass of a molecular ion or molecule calculated using the isotope
1085 mass of the most abundant constituent element isotope of each element rounded to
1086 the nearest integer value and multiplied by the number of atoms of each element.

- 1087
- 1088
- 1089
- 1090
- 1091
- 1092
- 1093
- 1094
- 1095
- 1096
- 1097
- 1098
- 1099
- 1100
- 1101
- 1102
- 1103
- *Resolution*. In a mass spectrum, the observed m/z value divided by the smallest difference $\Delta(m/z)$ for two ions that can be separated: $(m/z)/\Delta(m/z)$. The m/z value at which the measurement was made should be reported. The definition and method of measurement of $\Delta(m/z)$ should be reported. Commonly, this is performed using peak width measured at a specified percentage of peak height. Alternatively, $\Delta(m/z)$ is defined as the separation between two adjacent equal magnitude peaks such that the valley between them is a specified fraction of the peak height, for example as measured by peak matching.
 - *Resolving power*. Measure of the ability of a mass spectrometer to provide a specified value of mass resolution.
 - *Unified atomic mass unit (u)*. Non-SI unit of mass defined as one-twelfth of the mass of one atom of ^{12}C at rest in its ground state and equal to $1.660538921(73)\cdot 10^{-27}$ kg where the digits in parentheses indicate the estimated uncertainty in the final two digits of the value. Equivalent to the Dalton (Da) unit. The abbreviation amu for atomic mass unit is deprecated; it has been used to denote atomic masses measured relative to a single atom of ^{16}O , or to the isotope-averaged mass of an oxygen atom, or to a single atom of ^{12}C .

1104 2. SI. Local factors affecting the structure of the database

1105 The complete analyzed database consists of 152 samples and contains mass spectrometry
1106 data obtained from depositions of both soot and condensable gas on three different substrates:
1107 (1) binder-free, glass microfiber Whatman filters (21 mm diameter, 0.26 mm thickness,
1108 52 g m^{-2} , $0.7\text{ }\mu\text{m}$ smallest pore size purchased from Fisher Scientific), (2) Silicon (100) wafers
1109 (10x10x0.5 mm optically polished on one side purchased from PI-KEM Ltd) and (3) grade 5
1110 titanium alloy wafers (90% Ti, 6% Al, 4% V, 10x10x0.5 mm optically polished on one side
1111 purchased from Optics Concept).

1112 Fig. S1a shows the HCA output dendrogram, while the other three panels show the PCA
1113 output: Fig. S1b contains the PC1 vs. PC2 score plot and Fig. S1c and S1d contain the
1114 coefficient plots of the first two PCs vs. m/z . The database is reasonably well described with
1115 the first two PCs that together explain 67.3% of the total variance. In Fig. S1b the shape of the
1116 data points represents the deposition substrate: glass microfiber filters (round empty dots),
1117 silicon wafers (crosses) and titanium wafers (square solid dots). The clusters of samples

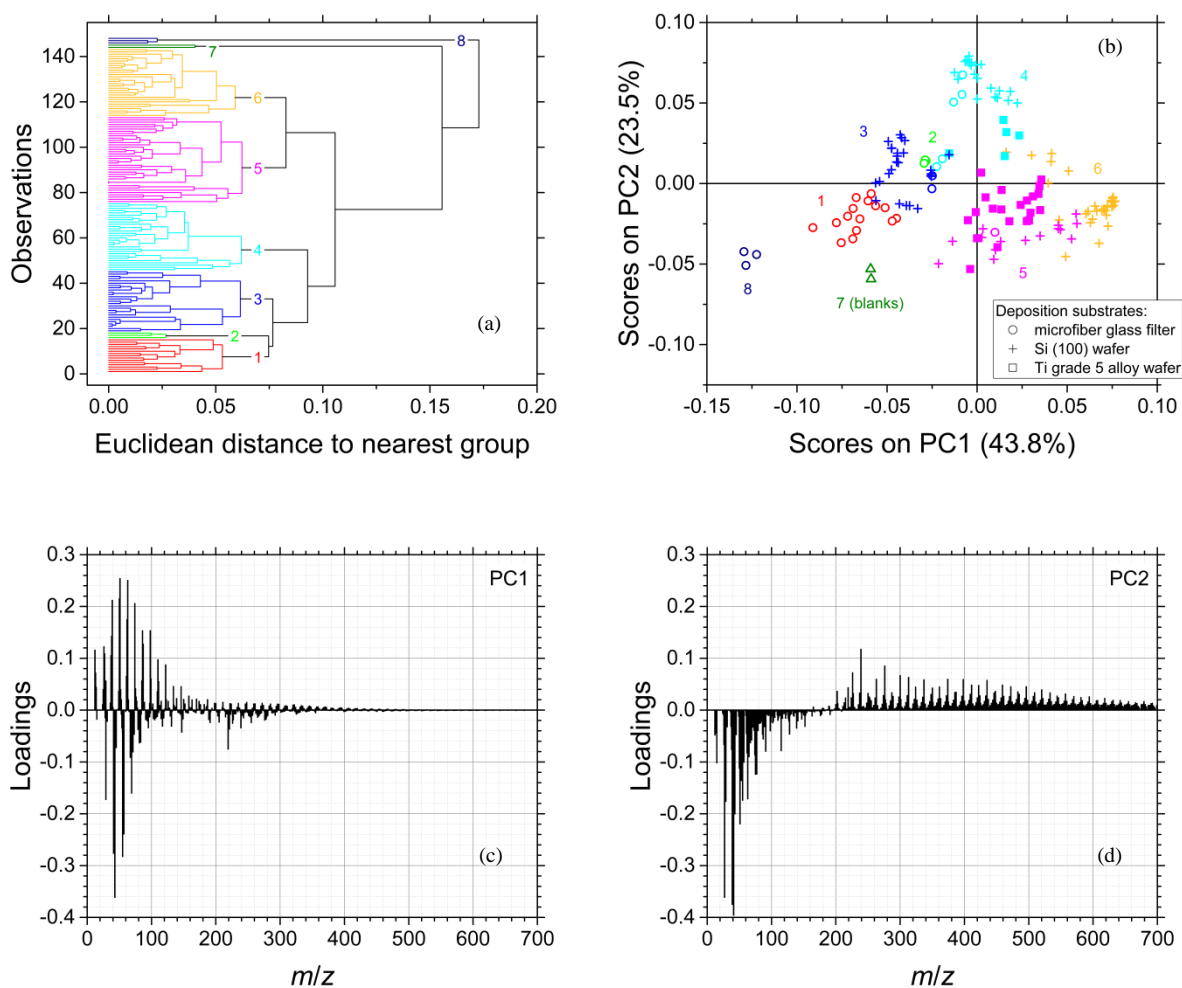
1118 identified by HCA are color-coded to match the data in the score plot. A satisfying agreement
1119 of HCA and PCA is found by following the data reduction procedure proposed in [73] that
1120 results in eight data clusters well separated and adjacent to each others in the score plot. The
1121 list of samples in each cluster can be found in Table S1. The analysis of the PC2 vs. PC1
1122 score plot reveals that all depositions on glass fiber filters but three (clusters 1, 2 and 8) and
1123 the depositions contaminated with organosilicon compounds (cluster 3) all appear at $PC1 < 0$,
1124 thus the deposition substrate and the presence of organosilicon contaminants rather than the
1125 nature of the samples give the main contribution (PC1, 43.8%) to the total variance of the
1126 database. More in detail:

- 1127 • a statistically significant difference exists between samples deposited on
1128 microfiber glass filters and on wafers. As shown in Fig. S1b, all samples obtained
1129 by deposition on microfiber glass filters (clusters 1, 2 and 8) appear at $PC1 < 0$. On
1130 the other hand, no statistically significant difference exists between samples
1131 deposited on silicon and titanium wafers once the mass spectra are normalized and
1132 the background peaks ($Si_xO_y^+$ and organosilicon ions in Si wafers, $Ti_xO_y^+$ and
1133 organotitanium ions in Ti wafers) are removed. To verify the equivalence of
1134 silicon and titanium wafers, ten samples are prepared in the same experimental
1135 conditions, five by deposition on silicon and five on titanium wafers. The intensity
1136 of the signals in the peak list are built into a scatter matrix and used to correlate
1137 each sample with all the samples obtained on the other substrate. The high
1138 correlation between intensities in the two groups (Pearson's coefficient variability
1139 range 0.81-0.98) and the absence of a significant separation in the score plots
1140 enforce the operational equivalence of silicon and titanium wafers as substrates for
1141 soot deposition;
- 1142 • significant amounts of organosilicon compounds were occasionally detected and
1143 attributed to uncontrolled thermal desorption from the conductive tubing for
1144 aerosol transport used in the early implementation of the sampling line [45]. This
1145 is a well known issue [88,89]. In our case, all the contaminated samples are
1146 grouped in cluster 3. Some of the depositions obtained from flame PRE-S before
1147 replacing the tubing were heavily contaminated and had to be discarded
1148 (underlined in Table S1). These samples were easy to recognize by visual
1149 inspection of the wafer surface due to the polysiloxane distinctive light

1150 polarization effect [45]. However, lighter contaminations are more difficult to
1151 identify. To this regard, PCA proved to be so effective that some other depositions
1152 were recognized as slightly contaminated only after PCA classified them in cluster
1153 3.

1154 This situation is less than ideal since high negative scores on PC1 (43.8%) correspond to
1155 samples affected by analytical and local factors, while the contribution of the hydrocarbons is
1156 relegated back to PC2 (23.5%) and even PC3 (11.8%). Therefore, to improve the quality of
1157 the data reduction, we removed from the database all the depositions on microfiber glass
1158 filters and the samples heavily contaminated with organosilicon compounds, and then
1159 re-analyzed the reduced data set (101 samples). The results of this second analysis are shown
1160 and discussed in the main text. Although at this stage it is rather difficult to obtain detailed
1161 information from the score plot, it is noteworthy that $PC2 > 0$ is mostly associated to PAH
1162 masses, as shown by the coefficients plot in Fig. S1d.

1163



1164 Fig. S1. Comparison of HCA and PCA. HCA dendrogram (a), score plots of the first two PCs (b), coefficients of PC1 (c)
 1165 and PC2 (d). The colors and numbers match the clusters in the two representations. In the score plot, round dots
 1166 represent depositions on microfiber glass filters, while crosses and square dots represent depositions on Si and Ti
 1167 wafers, respectively.

Cluster number	PRE-N	PRE-S	DIF-Q	DIF-S
1	7 gf, 12 gf, 15 gf, 20 gf	7 gf	/	/
2	/	15 gf	/	/
3	/	7 Si, <u>9 Si</u> , <u>12 Si</u> , <u>15 Si</u> 20 Si , 20 gf, 40 gf	/	/
4	15 gf, 40 gf	9 gf, 12 gf, 15 gf, 12 Ti	25 Si, 45 Si , 55 Si	48 Si, 65 Si
5	7 Si, 9 Si, 12 Si, 15 Si, 15 gf, 40 Si, 40 Ti	12 Ti, 15 Ti, 15 Ti , 20 Si, 40 Si, 40 Si	/	/
6	7 Si, 9 Si, 12 Si, 15 Si, 20 Si	40 Si	55 Si	65 Si, 80 Si, 80 Si
7 (blanks)	/	/	/	/
8	40 gf		/	/

1169 Table S1. Classification of samples based on HCA and PCA. The flames are listed in the columns while the cluster
1170 numbers in the rows. Each cell contains the sampled HAB followed by a two letter group indicating the deposition
1171 substrate (gf: microfiber glass filters, Si and Ti: wafers). Bold, normal and underlined text mark the samples obtained
1172 from the analysis of the soot spot (if present), the wafer surface and siloxane-contaminated, respectively.

3. SI. Database of identified ions

The four tables in this section list the 771 signals built into the main peak list and sorted by m/z by HCA. The peak list includes identified fragment ions (Table S2), signals that could not be reliably distinguished from the blank (Table S3) and hydrocarbons detected on soot and condensable gas with $PC1 < 0$ (nucleation in premixed flames, Table S4) and $PC1 > 0$ (nucleation in diffusion flames and surface growth, Table S5).

m/z	Formula	m/z	Formula	m/z	Formula	m/z	Formula	m/z	Formula
12.000	C ⁺	62.016	C ₅ H ₂ ⁺	121.008	C ₁₀ H ⁺	170.016	C ₁₄ H ₂ ⁺	235.040	/
13.008	CH ⁺	63.023	C ₅ H ₃ ⁺	122.016	C ₁₀ H ₂ ⁺	171.023	C ₁₄ H ₃ ⁺	246.016	/
14.016	CH ₂ ⁺	64.031	C ₅ H ₄ ⁺	123.023	C ₁₀ H ₃ ⁺	173.039	C ₁₄ H ₄ ⁺	247.024	/
15.023	CH ₃ ⁺	73.008	C ₆ H ⁺	124.031	C ₁₀ H ₄ ⁺	174.047	C ₁₄ H ₅ ⁺	248.047	/
24.000	C ₂ ⁺	74.016	C ₆ H ₂ ⁺	125.039	C ₁₀ H ₅ ⁺	175.055	C ₁₄ H ₆ ⁺	257.009	/
25.008	C ₂ H ⁺	75.023	C ₆ H ₃ ⁺	126.047	C ₁₀ H ₆ ⁺	176.063	C ₁₄ H ₇ ⁺	258.016	/
26.016	C ₂ H ₂ ⁺	76.031	C ₆ H ₄ ⁺	134.016	C ₁₁ H ₂ ⁺	182.016	C ₁₅ H ₂ ⁺	259.040	/
27.023	C ₂ H ₃ ⁺	85.008	C ₇ H ⁺	135.023	C ₁₁ H ₃ ⁺	183.023	C ₁₅ H ₃ ⁺	260.047	/
29.003	CHO ⁺	86.016	C ₇ H ₂ ⁺	136.031	C ₁₁ H ₄ ⁺	185.039	C ₁₅ H ₄ ⁺	270.016	/
36.000	C ₃ ⁺	87.023	C ₇ H ₃ ⁺	137.039	C ₁₁ H ₅ ⁺	186.032	C ₁₁ H ₆ O ₃ ⁺	271.024	/
37.008	C ₃ H ⁺	88.031	C ₇ H ₄ ⁺	138.047	C ₁₁ H ₆ ⁺	187.055	C ₁₅ H ₇ ⁺	272.047	/
38.016	C ₃ H ₂ ⁺	89.039	C ₇ H ₅ ⁺	139.055	C ₁₁ H ₇ ⁺	188.063	C ₁₅ H ₈ ⁺	281.009	/
39.023	C ₃ H ₃ ⁺	97.008	C ₈ H ⁺	145.008	C ₁₂ H ⁺	194.016	C ₁₆ H ₂ ⁺	282.016	/
40.031	C ₃ H ₄ ⁺	98.016	C ₈ H ₂ ⁺	146.016	C ₁₂ H ₂ ⁺	198.032	C ₁₂ H ₆ O ₃ ⁺	283.024	/
41.003	C ₂ HO ⁺	99.023	C ₈ H ₃ ⁺	147.023	C ₁₂ H ₃ ⁺	199.040	C ₁₂ H ₇ O ₃ ⁺	284.032	/
42.011	C ₂ H ₂ O ⁺	100.031	C ₈ H ₄ ⁺	148.031	C ₁₂ H ₄ ⁺	200.063	C ₁₆ H ₈ ⁺	296.032	/
48.000	C ₄ ⁺	101.039	C ₈ H ₅ ⁺	150.047	C ₁₂ H ₆ ⁺	209.024	/	305.01	/
49.008	C ₄ H ⁺	102.047	C ₈ H ₆ ⁺	151.055	C ₁₂ H ₇ ⁺	210.032	/	306.02	/
50.016	C ₄ H ₂ ⁺	109.008	C ₉ H ⁺	158.016	C ₁₃ H ₂ ⁺	211.040	/	328.99	/
51.023	C ₄ H ₃ ⁺	110.016	C ₉ H ₂ ⁺	159.023	C ₁₃ H ₃ ⁺	212.047	/	343.01	/
52.031	C ₄ H ₄ ⁺	111.023	C ₉ H ₃ ⁺	160.031	C ₁₃ H ₄ ⁺	222.032	/		
53.003	C ₃ HO ⁺	112.031	C ₉ H ₄ ⁺	161.039	C ₁₃ H ₅ ⁺	223.040	/		
60.000	C ₅ ⁺	113.039	C ₉ H ₅ ⁺	162.047	C ₁₃ H ₆ ⁺	233.009	/		
61.008	C ₅ H ⁺	114.047	C ₉ H ₆ ⁺	163.055	C ₁₃ H ₇ ⁺	234.016	/		

Table S2. Peaks attributed to fragment ions by HCA.

<i>m/z</i>	Formula	<i>m/z</i>	Formula	<i>m/z</i>	Formula	<i>m/z</i>	Formula	<i>m/z</i>	Formula
28.031	C ₂ H ₄ ⁺	55.055	C ₄ H ₇ ⁺	69.070	C ₅ H ₉ ⁺	82.042	C ₅ H ₆ O ⁺	97.065	C ₆ H ₉ O ⁺
29.039	C ₂ H ₅ ⁺	56.063	C ₄ H ₈ ⁺	70.042	C ₄ H ₆ O ⁺	82.078	C ₆ H ₁₀ ⁺	98.073	C ₆ H ₁₀ O ⁺
31.018	CH ₃ O ⁺	57.034	C ₃ H ₅ O ⁺	70.078	C ₅ H ₁₀ ⁺	83.086	C ₆ H ₁₁ ⁺	109.065	C ₇ H ₉ O ⁺
33.034	CH ₅ O ⁺	57.070	C ₄ H ₉ ⁺	71.050	C ₄ H ₇ O ⁺	84.058	C ₅ H ₈ O ⁺	109.102	C ₈ H ₁₃ ⁺
41.039	C ₃ H ₅ ⁺	65.039	C ₅ H ₅ ⁺	71.086	C ₅ H ₁₁ ⁺	84.094	C ₆ H ₁₂ ⁺	111.081	C ₇ H ₁₁ O ⁺
42.047	C ₃ H ₆ ⁺	66.047	C ₅ H ₆ ⁺	77.039	C ₆ H ₅ ⁺	91.018	C ₆ H ₃ O ⁺	115.018	C ₈ H ₃ O ⁺
43.018	C ₂ H ₃ O ⁺	67.018	C ₄ H ₃ O ⁺	78.047	C ₆ H ₆ ⁺	91.055	C ₇ H ₇ ⁺	117.034	C ₈ H ₅ O ⁺
43.055	C ₃ H ₇ ⁺	67.055	C ₅ H ₇ ⁺	79.018	C ₅ H ₃ O ⁺	92.026	C ₆ H ₄ O ⁺	131.050	C ₉ H ₇ O ⁺
45.034	C ₂ H ₅ O ⁺	68.026	C ₄ H ₄ O ⁺	79.055	C ₆ H ₇ ⁺	92.063	C ₇ H ₈ ⁺	131.086	C ₁₀ H ₁₁ ⁺
53.039	C ₄ H ₅ ⁺	68.063	C ₅ H ₈ ⁺	80.063	C ₆ H ₈ ⁺	93.070	C ₇ H ₉ ⁺	149.039	C ₁₂ H ₅ ⁺
54.047	C ₄ H ₆ ⁺	68.998	C ₃ HO ₂ ⁺	81.034	C ₅ H ₅ O ⁺	94.078	C ₇ H ₁₀ ⁺	155.086	C ₁₂ H ₁₁ ⁺
55.018	C ₃ H ₃ O ⁺	69.034	C ₄ H ₅ O ⁺	81.070	C ₆ H ₉ ⁺	95.086	C ₇ H ₁₁ ⁺		

Table S3. Peaks that could not be reliably distinguished from the blank.

<i>m/z</i>	Formula	<i>m/z</i>	Formula	<i>m/z</i>	Formula	<i>m/z</i>	Formula	<i>m/z</i>	Formula
90.047	C ₇ H ₆ ⁺	108.058	C ₇ H ₈ O ⁺	141.070	C ₁₁ H ₉ ⁺	170.094	C ₉ H ₁₄ O ₃ ⁺	219.081	C ₁₆ H ₁₁ O ⁺
93.034	C ₆ H ₅ O ⁺	108.094	C ₈ H ₁₂ ⁺	142.078	C ₁₁ H ₁₀ ⁺	177.070	C ₁₄ H ₉ ⁺	220.089	C ₁₆ H ₁₂ O ⁺
94.042	C ₆ H ₆ O ⁺	115.055	C ₉ H ₇ ⁺	143.086	C ₁₁ H ₁₁ ⁺	178.078	C ₁₄ H ₁₀ ⁺	220.183	C ₁₅ H ₂₄ O ⁺
95.050	C ₆ H ₇ O ⁺	116.063	C ₉ H ₈ ⁺	144.094	C ₁₁ H ₁₂ ⁺	180.094	C ₁₄ H ₁₂ ⁺	230.110	C ₁₈ H ₁₄ ⁺
96.058	C ₆ H ₈ O ⁺	117.070	C ₉ H ₉ ⁺	145.065	C ₁₀ H ₉ O ⁺	182.073	C ₁₃ H ₁₀ O ⁺	231.102	/
96.094	C ₇ H ₁₂ ⁺	118.042	C ₈ H ₆ O ⁺	146.073	C ₁₀ H ₁₀ O ⁺	189.070	C ₁₅ H ₉ ⁺	234.104	/
103.018	C ₇ H ₅ O ⁺	118.078	C ₉ H ₁₀ ⁺	152.063	C ₁₂ H ₈ ⁺	190.078	C ₁₅ H ₁₀ ⁺	242.094	/
103.055	C ₈ H ₇ ⁺	119.050	C ₈ H ₇ O ⁺	153.070	C ₁₂ H ₉ ⁺	191.086	C ₁₅ H ₁₁ ⁺	243.102	/
104.026	C ₇ H ₄ O ⁺	119.086	C ₉ H ₁₁ ⁺	154.078	C ₁₂ H ₁₀ ⁺	192.094	C ₁₅ H ₁₂ ⁺	244.110	/
104.063	C ₈ H ₈ ⁺	120.094	C ₉ H ₁₂ ⁺	156.094	C ₁₂ H ₁₂ ⁺	204.094	C ₁₆ H ₁₂ ⁺	245.118	/
105.034	C ₇ H ₅ O ⁺	127.055	C ₁₀ H ₇ ⁺	157.065	C ₁₁ H ₉ O ⁺	206.073	C ₁₅ H ₁₀ O ⁺	256.089	/
105.070	C ₈ H ₉ ⁺	128.063	C ₁₀ H ₈ ⁺	164.063	C ₁₃ H ₈ ⁺	214.078	C ₁₇ H ₁₀ ⁺	257.097	/
106.042	C ₇ H ₆ O ⁺	129.070	C ₁₀ H ₉ ⁺	166.078	C ₁₃ H ₁₀ ⁺	216.094	C ₁₇ H ₁₂ ⁺	258.104	/
106.078	C ₈ H ₁₀ ⁺	130.078	C ₁₀ H ₁₀ ⁺	167.086	C ₁₃ H ₁₁ ⁺	217.102	C ₁₇ H ₁₃ ⁺	268.110	/
107.050	C ₇ H ₇ O ⁺	132.094	C ₁₀ H ₁₂ ⁺	168.079	C ₉ H ₁₂ O ₃ ⁺	218.094	C ₁₃ H ₁₄ O ₃ ⁺		
107.086	C ₈ H ₁₁ ⁺	140.063	C ₁₁ H ₈ ⁺	169.086	C ₉ H ₁₃ O ₃ ⁺	218.167	C ₁₅ H ₂₂ O ⁺		

Table S4. Peaks attributed to soot and condensable gas by HCA and PCA (nucleation in premixed flames, PC1 < 0, see the loadings plots in Fig. 7).

<i>m/z</i>	Formula	<i>m/z</i>	Formula	<i>m/z</i>	Formula	<i>m/z</i>	Formula	<i>m/z</i>	Formula
165.070	C ₁₃ H ₉ ⁺	325.10	C ₂₆ H ₁₃ ⁺	414.14	C ₃₃ H ₁₈ ⁺	508.13	C ₄₁ H ₁₆ ⁺	601.0	/
179.086	C ₁₄ H ₁₁ ⁺	326.11	C ₂₆ H ₁₄ ⁺	415.01	/	509.13	C ₄₁ H ₁₇ ⁺	602.0	/
181.065	C ₁₃ H ₉ O ⁺	327.12	C ₂₆ H ₁₅ ⁺	415.13	/	510.14	C ₄₁ H ₁₈ ⁺	603.1	/
201.070	C ₁₆ H ₉ ⁺	328.13	C ₂₆ H ₁₆ ⁺	416.02	/	511.15	C ₄₁ H ₁₉ ⁺	604.1	/
202.078	C ₁₆ H ₁₀ ⁺	329.12	/	416.14	/	512.16	C ₄₁ H ₂₀ ⁺	605.1	C ₄₉ H ₁₇ ⁺
203.086	C ₁₆ H ₁₁ ⁺	330.00	/	417.03	/	513.16	C ₄₁ H ₂₁ ⁺	606.1	C ₄₉ H ₁₈ ⁺
205.065	C ₁₅ H ₉ O ⁺	330.13	/	418.03	/	514.02	/	607.1	C ₄₉ H ₁₉ ⁺
213.070	C ₁₇ H ₉ ⁺	331.01	/	419.04	/	515.03	/	608.2	C ₄₉ H ₂₀ ⁺
215.086	C ₁₇ H ₁₁ ⁺	331.13	/	420.05	/	516.03	/	609.2	C ₄₉ H ₂₁ ⁺
217.159	C ₁₅ H ₂₁ O ⁺	332.02	/	421.07	/	517.04	/	610.2	C ₄₉ H ₂₂ ⁺
219.175	C ₁₅ H ₂₃ O ⁺	333.04	/	422.11	C ₃₄ H ₁₄ ⁺	518.08	/	611.2	C ₄₉ H ₂₃ ⁺
221.118	/	334.05	/	423.12	C ₃₄ H ₁₅ ⁺	520.13	C ₄₂ H ₁₆ ⁺	612.0	/
222.126	/	335.07	/	424.13	C ₃₄ H ₁₆ ⁺	521.13	C ₄₂ H ₁₇ ⁺	612.2	C ₄₉ H ₂₄ ⁺
223.097	/	335.18	C ₂₆ H ₂₃ ⁺	425.13	C ₃₄ H ₁₇ ⁺	522.14	C ₄₂ H ₁₈ ⁺	613.0	/
224.047	/	336.08	/	426.14	C ₃₄ H ₁₈ ⁺	523.15	C ₄₂ H ₁₉ ⁺	614.0	/
225.055	/	337.10	C ₂₇ H ₁₃ ⁺	427.01	/	524.16	C ₄₂ H ₂₀ ⁺	615.1	/
226.078	C ₁₈ H ₁₀ ⁺	338.11	C ₂₇ H ₁₄ ⁺	427.15	C ₃₄ H ₁₉ ⁺	525.01	/	616.1	/
227.086	C ₁₈ H ₁₁ ⁺	339.12	C ₂₇ H ₁₅ ⁺	428.02	/	525.16	C ₄₂ H ₂₁ ⁺	617.1	/
228.094	C ₁₈ H ₁₂ ⁺	340.13	C ₂₇ H ₁₆ ⁺	428.16	C ₃₄ H ₂₀ ⁺	526.02	/	618.1	C ₅₀ H ₁₈ ⁺
229.102	C ₁₈ H ₁₃ ⁺	341.12	/	429.03	/	526.17	C ₄₂ H ₂₂ ⁺	619.1	C ₅₀ H ₁₉ ⁺
236.047	/	342.00	/	430.03	/	527.03	/	620.2	C ₅₀ H ₂₀ ⁺
237.070	C ₁₉ H ₉ ⁺	342.13	/	431.04	/	528.03	/	621.2	C ₅₀ H ₂₁ ⁺
238.078	C ₁₉ H ₁₀ ⁺	343.13	/	432.05	/	529.06	/	622.2	C ₅₀ H ₂₂ ⁺
239.086	C ₁₉ H ₁₁ ⁺	344.02	/	433.07	/	530.06	/	623.0	/
240.094	C ₁₉ H ₁₂ ⁺	345.04	/	435.12	C ₃₅ H ₁₅ ⁺	531.10	/	623.2	C ₅₀ H ₂₃ ⁺
241.102	C ₁₉ H ₁₃ ⁺	345.15	/	436.13	C ₃₅ H ₁₆ ⁺	532.11	/	624.0	/
246.104	C ₁₈ H ₁₄ O ⁺	346.03	/	437.13	C ₃₅ H ₁₇ ⁺	533.13	C ₄₃ H ₁₇ ⁺	624.2	C ₅₀ H ₂₄ ⁺
247.112	/	346.17	C ₂₇ H ₂₂ ⁺	438.14	C ₃₅ H ₁₈ ⁺	534.14	C ₄₃ H ₁₈ ⁺	625.0	/
249.055	/	347.06	/	439.15	C ₃₅ H ₁₉ ⁺	535.15	C ₄₃ H ₁₉ ⁺	626.0	/
250.078	C ₂₀ H ₁₀ ⁺	348.08	/	440.02	/	536.16	C ₄₃ H ₂₀ ⁺	627.0	/
251.086	C ₂₀ H ₁₁ ⁺	349.09	/	442.03	/	537.16	C ₄₃ H ₂₁ ⁺	629.1	/
252.094	C ₂₀ H ₁₂ ⁺	350.11	C ₂₈ H ₁₄ ⁺	443.04	/	538.02	/	630.1	/
253.102	C ₂₀ H ₁₃ ⁺	351.12	C ₂₈ H ₁₅ ⁺	444.05	/	538.17	C ₄₃ H ₂₂ ⁺	631.1	C ₅₁ H ₁₉ ⁺
254.110	C ₂₀ H ₁₄ ⁺	352.13	C ₂₈ H ₁₆ ⁺	445.06	/	539.03	/	632.2	C ₅₁ H ₂₀ ⁺
255.081	/	353.13	C ₂₈ H ₁₇ ⁺	446.06	/	539.18	C ₄₃ H ₂₃ ⁺	633.2	C ₅₁ H ₂₁ ⁺
261.055	/	354.14	C ₂₈ H ₁₈ ⁺	447.12	C ₃₆ H ₁₅ ⁺	540.03	/	634.2	C ₅₁ H ₂₂ ⁺
262.063	/	354.29	C ₂₅ H ₃₈ O ⁺	448.13	C ₃₆ H ₁₆ ⁺	541.04	/	635.2	C ₅₁ H ₂₃ ⁺
262.230	C ₁₈ H ₃₀ O ⁺	355.01	/	449.13	C ₃₆ H ₁₇ ⁺	542.05	/	636.0	/
263.086	C ₂₁ H ₁₁ ⁺	355.13	/	450.14	C ₃₆ H ₁₈ ⁺	543.06	/	636.2	C ₅₁ H ₂₄ ⁺
264.094	C ₂₁ H ₁₂ ⁺	355.30	C ₂₅ H ₃₉ O ⁺	451.01	/	544.13	C ₄₄ H ₁₆ ⁺	637.0	/
264.245	C ₁₈ H ₃₂ O ⁺	356.02	/	451.15	C ₃₆ H ₁₉ ⁺	545.13	C ₄₄ H ₁₇ ⁺	637.2	C ₅₁ H ₂₅ ⁺
265.102	C ₂₁ H ₁₃ ⁺	357.03	/	452.14	/	546.14	C ₄₄ H ₁₈ ⁺	638.0	/
265.253	C ₁₈ H ₃₃ O ⁺	358.05	/	453.01	/	547.15	C ₄₄ H ₁₉ ⁺	639.0	/

266.110	C ₂₁ H ₁₄ ⁺	359.04	/	454.02	/	548.16	C ₄₄ H ₂₀ ⁺	640.1	/
267.117	C ₂₁ H ₁₅ ⁺	360.06	/	455.03	/	549.16	C ₄₄ H ₂₁ ⁺	641.1	/
269.118	/	361.10	C ₂₉ H ₁₃ ⁺	456.03	/	550.17	C ₄₄ H ₂₂ ⁺	642.1	C ₅₂ H ₁₈ ⁺
270.126	/	362.11	C ₂₉ H ₁₄ ⁺	457.06	/	551.03	/	643.1	C ₅₂ H ₁₉ ⁺
271.112	/	363.12	C ₂₉ H ₁₅ ⁺	458.06	/	551.18	C ₄₄ H ₂₃ ⁺	644.2	C ₅₂ H ₂₀ ⁺
273.055	/	364.13	C ₂₉ H ₁₆ ⁺	459.12	C ₃₇ H ₁₅ ⁺	552.03	/	645.2	C ₅₂ H ₂₁ ⁺
274.078	C ₂₂ H ₁₀ ⁺	365.13	C ₂₉ H ₁₇ ⁺	460.13	C ₃₇ H ₁₆ ⁺	552.19	C ₄₄ H ₂₄ ⁺	646.2	C ₅₂ H ₂₂ ⁺
275.086	C ₂₂ H ₁₁ ⁺	366.00	/	461.13	C ₃₇ H ₁₇ ⁺	553.04	/	647.2	C ₅₂ H ₂₃ ⁺
276.094	C ₂₂ H ₁₂ ⁺	366.13	/	462.14	C ₃₇ H ₁₈ ⁺	554.05	/	648.2	C ₅₂ H ₂₄ ⁺
277.102	C ₂₂ H ₁₃ ⁺	367.01	/	463.15	C ₃₇ H ₁₉ ⁺	555.06	/	649.0	/
278.110	C ₂₂ H ₁₄ ⁺	368.02	/	464.02	/	556.06	/	651.1	/
278.261	C ₁₉ H ₃₄ O ⁺	369.03	/	464.16	C ₃₇ H ₂₀ ⁺	557.13	C ₄₅ H ₁₇ ⁺	652.1	/
279.117	C ₂₂ H ₁₅ ⁺	370.03	/	465.03	/	558.14	C ₄₅ H ₁₈ ⁺	653.1	C ₅₃ H ₁₇ ⁺
279.269	C ₁₉ H ₃₅ O ⁺	371.04	/	465.16	C ₃₇ H ₂₁ ⁺	559.15	C ₄₅ H ₁₉ ⁺	654.1	C ₅₃ H ₁₈ ⁺
285.055	/	372.06	/	466.02	/	560.16	C ₄₅ H ₂₀ ⁺	655.1	C ₅₃ H ₁₉ ⁺
286.063	/	373.07	/	467.03	/	561.16	C ₄₅ H ₂₁ ⁺	656.2	C ₅₃ H ₂₀ ⁺
287.086	C ₂₃ H ₁₁ ⁺	374.11	C ₃₀ H ₁₄ ⁺	468.03	/	562.02	/	657.2	C ₅₃ H ₂₁ ⁺
287.180	C ₂₂ H ₂₃ ⁺	375.12	C ₃₀ H ₁₅ ⁺	469.07	/	562.17	C ₄₅ H ₂₂ ⁺	658.2	C ₅₃ H ₂₂ ⁺
288.094	C ₂₃ H ₁₂ ⁺	376.13	C ₃₀ H ₁₆ ⁺	470.09	/	563.03	/	659.2	C ₅₃ H ₂₃ ⁺
289.102	C ₂₃ H ₁₃ ⁺	377.13	C ₃₀ H ₁₇ ⁺	471.10	/	563.18	C ₄₅ H ₂₃ ⁺	660.0	/
290.110	C ₂₃ H ₁₄ ⁺	378.14	C ₃₀ H ₁₈ ⁺	472.13	C ₃₈ H ₁₆ ⁺	564.03	/	660.2	C ₅₃ H ₂₄ ⁺
290.261	C ₂₀ H ₃₄ O ⁺	379.01	/	473.13	C ₃₈ H ₁₇ ⁺	565.04	/	662.0	/
291.117	C ₂₃ H ₁₅ ⁺	379.13	/	474.14	C ₃₈ H ₁₈ ⁺	566.05	/	664.1	/
292.277	C ₂₀ H ₃₆ O ⁺	380.03	/	475.15	C ₃₈ H ₁₉ ⁺	567.06	/	665.1	/
293.118	/	381.03	/	476.16	C ₃₈ H ₂₀ ⁺	568.08	/	666.1	C ₅₄ H ₁₈ ⁺
293.284	C ₂₀ H ₃₇ O ⁺	382.03	/	477.01	/	569.09	/	667.1	C ₅₄ H ₁₉ ⁺
294.016	/	383.06	/	477.16	C ₃₈ H ₂₁ ⁺	570.14	C ₄₆ H ₁₈ ⁺	668.2	C ₅₄ H ₂₀ ⁺
294.126	/	384.06	/	478.02	/	571.15	C ₄₆ H ₁₉ ⁺	669.2	C ₅₄ H ₂₁ ⁺
295.024	/	385.10	C ₃₁ H ₁₃ ⁺	478.17	C ₃₈ H ₂₂ ⁺	572.16	C ₄₆ H ₂₀ ⁺	670.2	C ₅₄ H ₂₂ ⁺
295.133	/	386.11	C ₃₁ H ₁₄ ⁺	479.03	/	573.16	C ₄₆ H ₂₁ ⁺	671.2	C ₅₄ H ₂₃ ⁺
297.040	/	387.12	C ₃₁ H ₁₅ ⁺	481.06	/	574.17	C ₄₆ H ₂₂ ⁺	672.2	C ₅₄ H ₂₄ ⁺
298.063	/	388.13	C ₃₁ H ₁₆ ⁺	482.06	/	575.03	/	675.1	/
299.071	/	389.13	C ₃₁ H ₁₇ ⁺	483.12	C ₃₉ H ₁₅ ⁺	575.18	C ₄₆ H ₂₃ ⁺	677.1	/
300.094	C ₂₄ H ₁₂ ⁺	390.00	/	484.13	C ₃₉ H ₁₆ ⁺	576.03	/	679.1	C ₅₅ H ₁₉ ⁺
301.10	C ₂₄ H ₁₃ ⁺	390.13	/	485.13	C ₃₉ H ₁₇ ⁺	577.04	/	680.2	C ₅₅ H ₂₀ ⁺
302.11	C ₂₄ H ₁₄ ⁺	391.01	/	486.14	C ₃₉ H ₁₈ ⁺	578.05	/	681.2	C ₅₅ H ₂₁ ⁺
303.12	C ₂₄ H ₁₅ ⁺	391.13	/	487.15	C ₃₉ H ₁₉ ⁺	579.07	/	682.2	C ₅₅ H ₂₂ ⁺
304.13	C ₂₄ H ₁₆ ⁺	392.02	/	488.02	/	580.08	/	683.2	C ₅₅ H ₂₃ ⁺
305.12	/	393.03	/	488.16	C ₃₉ H ₂₀ ⁺	581.13	C ₄₇ H ₁₇ ⁺	686.0	/
306.13	/	394.03	/	489.03	/	582.14	C ₄₇ H ₁₈ ⁺	688.0	/
307.02	/	395.04	/	489.16	C ₃₉ H ₂₁ ⁺	583.15	C ₄₇ H ₁₉ ⁺	690.1	/
307.13	/	396.06	/	490.02	/	584.16	C ₄₇ H ₂₀ ⁺	691.1	/
308.03	/	397.07	/	491.04	/	585.16	C ₄₇ H ₂₁ ⁺	692.2	C ₅₆ H ₂₀ ⁺
308.14	/	398.11	C ₃₂ H ₁₄ ⁺	492.05	/	586.17	C ₄₇ H ₂₂ ⁺	693.2	C ₅₆ H ₂₁ ⁺

309.04	/	399.12	C ₃₂ H ₁₅ ⁺	493.06	/	587.03	/	694.2	C ₅₆ H ₂₂ ⁺
310.06	/	400.13	C ₃₂ H ₁₆ ⁺	494.06	/	587.18	C ₄₇ H ₂₃ ⁺	695.2	C ₅₆ H ₂₃ ⁺
311.07	/	401.13	C ₃₂ H ₁₇ ⁺	495.09	/	588.03	/	696.2	C ₅₆ H ₂₄ ⁺
312.09	C ₂₅ H ₁₂ ⁺	402.14	C ₃₂ H ₁₈ ⁺	496.13	C ₄₀ H ₁₆ ⁺	589.04	/	699.1	/
313.10	C ₂₅ H ₁₃ ⁺	403.01	/	497.13	C ₄₀ H ₁₇ ⁺	590.05	/	701.1	/
314.11	C ₂₅ H ₁₄ ⁺	403.15	C ₃₂ H ₁₉ ⁺	498.14	C ₄₀ H ₁₈ ⁺	591.06	/	703.1	C ₅₇ H ₁₉ ⁺
315.12	C ₂₅ H ₁₅ ⁺	404.02	/	499.15	C ₄₀ H ₁₉ ⁺	592.08	/	704.2	C ₅₇ H ₂₀ ⁺
316.13	C ₂₅ H ₁₆ ⁺	405.03	/	500.16	C ₄₀ H ₂₀ ⁺	593.09	/	705.2	C ₅₇ H ₂₁ ⁺
317.13	C ₂₅ H ₁₇ ⁺	406.03	/	501.03	/	594.14	C ₄₈ H ₁₈ ⁺	706.2	C ₅₇ H ₂₂ ⁺
318.13	/	407.04	/	501.16	C ₄₀ H ₂₁ ⁺	595.15	C ₄₈ H ₁₉ ⁺	707.2	C ₅₇ H ₂₃ ⁺
319.01	/	408.05	/	502.03	/	596.16	C ₄₈ H ₂₀ ⁺	716.2	C ₅₈ H ₂₀ ⁺
319.13	/	409.09	/	502.17	C ₄₀ H ₂₂ ⁺	597.16	C ₄₈ H ₂₁ ⁺	717.2	C ₅₈ H ₂₁ ⁺
320.02	/	410.09	/	503.03	/	598.17	C ₄₈ H ₂₂ ⁺	718.2	C ₅₈ H ₂₂ ⁺
321.03	/	411.12	C ₃₃ H ₁₅ ⁺	504.03	/	599.03	/	729.2	C ₅₉ H ₂₁ ⁺
322.05	/	412.13	C ₃₃ H ₁₆ ⁺	505.06	/	599.18	C ₄₈ H ₂₃ ⁺	731.2	C ₅₉ H ₂₃ ⁺
323.06	/	413.13	C ₃₃ H ₁₇ ⁺	506.06	/	600.03	/		
324.09	C ₂₆ H ₁₂ ⁺	414.00	/	507.10	/	600.2	C ₄₈ H ₂₄ ⁺		

Table S5. Peaks attributed to soot and condensable gas by HCA and PCA (nucleation in premixed flames and surface growth, PC1 > 0, see the loadings plots in Fig. 7).

4. SI. References

- [87] K.K. Murray, R.K. Boyd, M.N. Eberlin, G.J. Langley, L. Li, Y. Naito, Definitions of terms relating to mass spectrometry (IUPAC Recommendations 2013), *Pure Appl Chem.* 85 (2013) 1515–1609.
- [88] M.T. Timko, Z. Yu, J. Kroll, J.T. Jayne, D.R. Worsnop, R.C. Miake-Lye, T.B. Onasch, D. Liscinsky, T.W. Kirchstetter, H. Destailats, A.L. Holder, J.D. Smith, K.R. Wilson, Sampling artifacts from conductive silicone tubing, *Aerosol Sci. Technol.* 43 (2009) 855–865. doi:10.1080/02786820902984811.
- [89] Y. Yu, M. Liz Alexander, V. Perraud, E.A. Bruns, S.N. Johnson, M.J. Ezell, B.J. Finlayson-Pitts, Contamination from electrically conductive silicone tubing during aerosol chemical analysis, *Atmos. Environ.* 43 (2009) 2836–2839. doi:10.1016/j.atmosenv.2009.02.014.